12-2009

Manganese oxide mineral phases produced at room temperature under acidic conditions investigated with XRD, TEM, SEM, EDS, and BET

Nancy R. Birkner
University of Nevada Las Vegas

MANGANESE OXIDE MINERAL PHASES PRODUCED AT ROOM TEMPERATURE UNDER ACIDIC CONDITIONS INVESTIGATED WITH XRD, TEM, SEM, EDS, AND BET

by

Nancy R. Birkner

Bachelor of Arts
University of Nevada, Las Vegas
1993

A thesis document submitted in partial fulfillment of
the requirements for the

Master of Science in Chemistry
Department of Chemistry
College of Sciences

Graduate College
University of Nevada, Las Vegas
December 2009

UNLV
UNIVERSITY OF NEVADA LAS VEGAS

The Graduate College

We recommend that the thesis prepared under our supervision by

Nancy R. Birkner

entitled

Manganese Oxide Mineral Phases Produced at Room Temperature Under Acidic Conditions Investigated with XRD, TEM, SEM, EDS, and BET

be accepted in partial fulfillment of the requirements for the degree of

Master of Science
Chemistry

Spencer M. Steinberg, Committee Chair

Thomas Hartmann, Committee Member

Longzhou Ma, Committee Member

Dennis W. Lindle, Committee Member

Clemens Heske, Committee Member

Andrew Cornelius, Graduate Faculty Representative

Ronald Smith, Ph. D., Vice President for Research and Graduate Studies
and Dean of the Graduate College

December 2009

ABSTRACT

Manganese Oxide Mineral Phases Produced at Room Temperature under Acidic Conditions Investigated with XRD, TEM, SEM, EDS, and BET

by

Nancy R. Birkner

Dr. Spencer M. Steinberg, Examination Committee Chair
Professor of Chemistry
University of Nevada, Las Vegas

This thesis concerns characterization of synthetic manganese oxides belonging to mineral phases known as Birnessite and Cryptomelane. Presented here are the results of an experiment designed to examine the influence of sodium, potassium, chloride, and sulfate ions on the reduction of potassium permanganate under acidic conditions at room temperature to produce Birnessite and Cryptomelane. The experiments used $KMnO_4$ as the source of Mn and the resulting Birnessite and Cryptomelane precipitates were washed with 18 MΩ/cm NANOpure water at the end of syntheses. Several state-of-the-art solid state techniques were used to characterize the Mn-based oxide mineral phases. Based on the literature review, our prior research, and solid state characterization of the final products, some correlations between the reactions and the resulting mineral phases that were formed have been explored in the discussion section.

TABLE OF CONTENTS

TABLE OF FIGURES

ACKNOWLEDGEMENTS

Grateful acknowledgements for graduate and research financial support for this Master of Science Degree in Chemistry go out to Anthony Hechanova, Oliver Hemmers, Thomas Hartmann, and Spencer Steinberg. Thank you for guidance in the theory and application of XRD (Thomas Hartmann), S/TEM (Longzhou Ma), SEM, EDS and WDS (Robert Fairhurst). Much appreciation to Clayton Crow, of the X-Ray Diffraction and X-ray Fluorescence Laboratory (XXL) and Electron Microanalysis Instrumentation Laboratory (EMIL) of the Geoscience department at the University of Nevada - Las Vegas, Nevada; to the Structure and Solid Phase Group (S-SPA) of the Harry Reid Center in Las Vegas, Nevada; to Iraida N. Demchenko and Wayne C. Stolte of the Lawrence Berkeley National Laboratory Advanced Light Source (LBNL-ALS); and to Robert J. Fairhurst of the Camborne School of Mines, University of Exeter, UK, for their excellent support, considerations, and technical consultations. Thank you to Distinguished Professor Steve Suib, Department of Chemistry at the University of Connecticut, for thoughtful collaboration. Thank you to Distinguished Professor Alexandra Navrotsky, Director, Peter A. Rock Thermochemistry Laboratory and NEAT ORU, University of California - Davis, for providing a place for me and my little manganese oxides, but most of all for providing me with mentorship and support as I continue my education under your guidance in the Chemistry Ph.D. program at UC-Davis. Thank you to my parents, Everett and Patsy Birkner, for all sorts of wonderful things that great parents provide to their children, but mainly for your unconditional love, encouragement, and for proof-reading my manuscripts when my eyes were too tired to focus.

CHAPTER 1

INTRODUCTION

Manganese-based mineral oxides, as produced in the natural environment, are found in soil, sediment, and rock patina (e. g. Desert Varnish). Synthetic manganese-based oxides have been produced for research and industry for many decades [1,2,3]. Polymorphs of MnO_2 (collectively termed Mn-oxides) include multiple classes [4,5] which are comprised of tunnel-structure (e.g. Cryptomelane) and layer-structure (e.g. Birnessite).

Cryptomelane belongs to the class of tunnel-structure type Mn-oxide polymorphs. The tunnels possess internal sizes commensurate with cations to which they are host. These tunnels are the basis for molecular sieve technology [6], from which the common name octahedral molecular sieves (OMS) was acquired. Organic synthesis has also found use for Cryptomelane due to its mild catalytic properties [7,8]. Cryptomelane is derived from the Greek for hidden and black, alluding to the mineral's obscure identity as one of several black mineral species in "psilomelane", the collective term for hard manganese oxides [9].

Birnessite belongs to another class of Mn-oxide polymorphs, which possess a layered-type (lamellar) structure. Because of their easily recognizable morphology, Birnessite-type materials are also referred to as octahedral layered structures (OLS) [10,11]. Synthetic Birnessite-type (OLS) materials are of interest because their electron transfer (or redox) properties are useful to solid-state battery systems [12]. In addition, the semiconducting and magnetic properties [13] have been applied to magnetic storage. Birnessite is a name that hails from Birness, Aberdeenshire, Scotland. It was here, in

1956, that a husband-and-wife team of mineralogists, L.H.P. Jones and Angela Milne, [14] were exploring a fluvio-galcial gravel deposit, when they discovered an interesting and unfamiliar rock. Upon analysis, Milne and Jones learned that they had discovered a new manganese-based mineral oxide, which they named Birnessite after the location of its find. It has since been learned that Birnessite is one of the most common forms of manganese-based oxides found in soils [15,16].

Cryptomelane and Birnessite have been studied for their interesting properties, which include heavy metal sorption, volatile organic pollutant decomposition, remediation of ground water pollutants, and acting as natural barriers against radioisotope migration through soil. Cryptomelane and Birnessite, although important to various advanced material technologies, are not well understood in terms of synthetic parameter influence on phase formation (or transformation as the case may be). The literature describes many methods for preparing Mn-based-oxide materials. However, there are research questions, such as, what parameters influence the formation of layer-structure (Birnessite) versus tunnel-structure (Cryptomelane) Mn-oxide polymorphs. Indeed, recent contributions have been made in the field toward synthetic influence of manganese-based metal oxide microstructure and nanostructure to promote desirable properties for research and industry [17,18,19,20]. Conversely, few examples exist where synthetic conditions are systematically varied to study patterns of influence on Mn-based metal oxide phase formation/transformation.

One such example is a recent publication, which presented an elegantly designed experiment done with *in situ* X-Ray Diffraction (XRD) to follow the phase transformation from layer-structure type Mn-oxide (Birnessite) to tunnel-structure type

Mn-oxide (Cryptomelane) under refluxing and acidic conditions as a function of time [21]. Jonaslet Villegas et al., 2005, studied the influence of a single parameter change (pH) on the transformation of Mn-oxide phase from OLS to OMS under two different acidic solution reaction conditions (buffered pH versus non-buffered pH) in the presence of applied heat. The underlying reaction was Mn(II) oxidation (oxidized by hydrogen peroxide). The single parameter variation was time during which two reaction conditions were explored that included a buffered media that was slightly acidic at pH = 4.5 and a non-buffered acidic media at pH = 2. Another recent study of Mn-based metal oxide phase formation/transformation can be found in a publication in which time-resolved Synchrotron XRD was used to study the development of phases and crystal structure during cation exchange reactions of synthetic Na-Birnessite [22].

Researchers in the field of Mn-oxide continue to search for influences on transformation/formation of tunnel-type versus layered-type Mn-oxide mineral phases. Previously, we reported product formation rates for the Cryptomelane [23] and Birnessite [24] formed from classic techniques (McKenzie, 1971). Moreover, in the presence of applied heat both of these reported products formed in 4 h; reproducibility reactions showed that the same products formed in 2 h by increasing the drop-wise rate of addition part of the procedure. Additionally, the Cryptomelane mineral phase formed during the decomposition of permanganate and concentrated sulfuric acid [25], the reaction, which we previously reported, began vigorously and then progressed slowly for about a week-and-a-half. Therefore, the current study was designed to explore other parameters that were, basically, the remaining culprits (the cations and anions that were involved in our earlier studies). The classic method we used to produce Birnessite (McKenzie, 1971)

involved permanganate, HCl, and applied temperature. The classic method we used to produce Cryptomelane (McKenzie, 1971) involved manganous sulfate ($Mn(II)SO_4$), acetic acid, permanganate, and applied heat. To narrow the list of possible reaction parameter influences that promote the formation of Cryptomelane or Birnessite, then remove the most obvious player first, which was the applied temperature (McKenzie, 1971, the temperatures used to produce Cryptomelane was 75 ^oC, and 100 ^oC was used for Birnessite); thus, our samples were produced at room temperature. Then it was important to isolate the specific cations (K^+; Na^+ was used as a comparator) and anions (Cl^- versus HSO_4^-) to determine what their relationship to product formation might be. Although we had used $Mn(II)SO_4$ in previous experiments, for the present study we avoided the use of Mn(II) in order to realize the influence of K^+ or Na^+ in the reaction matrix. One widely held assumption is that Mn(II) is an important component in the formation of the Cryptomelane product. Additionally, we wanted to determine if the sulfate of the manganous sulfate ($MnSO_4$) rather than the Mn(II) was the influence on Cryptomelane formation. Thus, in the current investigation, we specifically chose not use *manganous* forms of the salt (e.g. Mn(II), such as, $MnSO_4$ or $MnCl_2$) due to the ability of manganese in its reduced form to interfere through sorption at the mineral oxide surface. Moreover, limited by funding, we could only select the most likely candidates for study. Furthermore, by removing applied heat and Mn(II) we could indirectly rule these parameter out if we formed the Birnessite and Cryptomelane products. The reaction parameters chosen for exploration in this project included cations using concentrated alkali chloride salts of NaCl or KCl and anions using HCl versus sulfuric acid. We proposed the comparison of group-VII anion (chloride), group-VI anion (sulfate), and

group-I cations (sodium and potassium). The method of solid formation was reduction of potassium permanganate under acidic conditions at room temperature. Characterizations of the resulting precipitated Mn-oxide products were used to correlate reaction parameter influence on crystal phase structure-type formation.

The samples produced in the research presented here are Mn-oxide-based products of Cryptomelane or Birnessite. The products were characterized to identify mineralogical phase, specific surface area, morphology, and imaging of micro- and nano-structure. The data was used to correlate the product changes with the single parameter variation. An example of Cryptomelane sample produced in the current research is designated V1P78D. Additionally, examples of Birnessite produced in this research are designated V1P76A, V1P76B, and V1P77C. The purpose of the current research is to observe the effect of parameter variations on phase formation, microstructure, and morphology of synthetic Mn-oxide mineral phases (e.g. Birnessite and Cryptomelane). The products were characterized using X-ray Diffraction (XRD), Transmission Electron Microscopy (TEM), Scanning Electron Microscopy (SEM), Energy Dispersive Spectroscopy (EDS), and Brunauer-Emmett-Teller (BET) method for specific surface area analysis (BET).

CHAPTER 2

BACKGROUND REVIEW

2.1 Elemental Manganese

The abbreviation for elemental manganese is Mn. In the periodic table, the position of Mn is period IV subgroup VII. Mn, a transition metal, has atomic number 25, atomic mass 54.938 g/mol, and electron configuration [Ar] $4s^2 3d^5$. Mn-based species owe their interesting properties to their 3d orbitals, which hybridize with 4s and 3p orbitals [26,27,28]. When fully coordinated with oxygen atoms, Mn has coordination number 6. The result is the metal oxide octahedral unit.

2.2 Chemical Behavior of Manganese

Mn is capable of oxidation states ranging from +2 -to- +7, however, common oxidation states of Mn-oxide are non-stoichiometric [29]. Mn(II, III) species behave as Lewis acids, whereas higher average oxidation states, such as Mn(V,VI,VII), portray Lewis base behavior [30]. Depending on the environment to which it is exposed, amphoteric behavior is expected of Mn(IV), which means it may behave as a Lewis base or Lewis acid [31, 32].

2.3 pH Influence on Behavior of Nanoparticle Surfaces

pH may have influence on behavior of nanoparticle surfaces. Point of Zero Charge (PZC) is the pH at which a surface potential falls to zero. Theoretically, the PZC and nanoparticle surface potential may be estimated using the equation E(volts) = 0.059[PZC-pH], which implies dependence of nanoparticle surface energy on local environment pH [33]. This suggests nanoparticle surface potential may be influenced by pH, perhaps to promote expression of desired surface behavior. Manganese-oxide surfaces have active

sites, which are responsible for surface potential. It has been reported that hydroxyl ions of nanoparticle Mn-oxide surfaces are considered the active sites for substrate adsorption [34,35]. Additionally, in an acidic solution matrix, exposed surface active sites (-OH groups) of Mn-oxide surfaces will be protonated. Thus, under acidic conditions, Mn-oxide species display Lewis base behavior.

2.4 Cation Influence on Mn-Oxide Mineral Formation and Nanoparticle Surfaces

Cations may have influence on Mn-oxide crystal phase formation and nanoparticle surfaces. Mn-oxide surfaces express adsorptive behavior toward cations [36,37,38,39]. In the presence of a cation, the polar, negatively-charged regions distributed about a soluble Mn-oxide coordinate complex are cation-bridged to additional such Mn-oxide coordinate species [40,41]. Additionally, cations adsorb to metal-oxide surfaces from the diffuse swarm. Consequently, as the cation complexes at the surface of the metal oxide, a new layer of hydroxide may form or, similarly, additional metal-oxide surfaces may be attracted and subsequently layer atop the cation-metal-oxide complex [42].

2.5 Anion Influence on Mn-Oxide Mineral Formation and Nanoparticle Surfaces

Anions may have influence on Mn-oxide crystal phase formation and nanoparticle surfaces. It is known that group VI elements will complex with neighboring species under reducing conditions (e.g. in this research potassium permanganate was reduced) whereas group VII elements will not [43,44,45,46]. Therefore, given similar reducing conditions there exists a possibility that these group differences may be used to study promotion of crystal phases. Variation of the concentration of the anions may also be used to determine whether the influence is promoted by outer-sphere complexation, as this mechanism is based on electrostatic bonding [47].

CHAPTER 3

METHODOLOGY

3.1 Synthesis Method and Sample

Overall, the synthetic method involved reduction of potassium permanganate in solution, developed from literature reviews [[48]]. The use of mass- and electron-balanced redox reaction equations were used to determine the reaction concentrations for the experiments shown in equations 1-3.

$6\ Cl^- \rightarrow 3\ Cl_2 + 6\ e^-$ $E° = -1.358\ V$ (1)

$2\ MnO_4^- + 6\ e^- + 8\ H^+ \rightarrow 2\ MnO_2 + 4\ H_2O$ $E° = +1.67\ V$ (2)

$2\ MnO_4^- + 6\ Cl^- + 8\ H^+ \rightarrow 2\ MnO_2 + 3\ Cl_2 + 4\ H_2O$ $E° = +0.31\ V$ (3)

Thus, for the spontaneous room temperature reaction redox couple, use was made of $1\ MnO_4^-$: $3\ Cl^-$: $4\ H^+$. Chloride spontaneously reduces the $KMn(VII)O_4$ to produce the birnessite and cryptomelane products. The syntheses to produce samples V1P76B, V1P77C, and V1P78D involved room temperature reduction of potassium permanganate under acidic conditions (pH = -log[0.5] = 0.3) to influence the production of Birnessite-type Mn-oxide phases. The parameter variation between reactions V1P77C and V1P76B included the addition of concentrated (3.00 M) alkali-chloride salt (NaCl, KCl), which provided the high chloride concentration in addition to providing cation species (Na^+, K^+). Reaction V1P76A was run as a control for these reactions by not adding concentrated alkali chloride to the matrix. The specific synthesis of V1P76B sample included drop-wise addition of 0.500 M hydrochloric acid into a solution of 0.125 M potassium permanganate, which had been completely dissolved into an aqueous 3.00 M

sodium chloride (NaCl) salt solution. The specific synthesis of V1P77C sample included drop-wise addition of 0.500 M hydrochloric acid into a solution of 0.125 M potassium permanganate, which had been dissolved into an aqueous 3.00 M potassium chloride salt (KCl) solution. The specific synthesis of V1P78D sample included drop-wise addition of 0.500 M sulfuric acid (pH = -log[0.5] = 0.3; pH adjusted with HCl) into a solution of 0.125 M potassium permanganate, which had been dissolved into an aqueous 3.00 M sodium chloride (NaCl) salt solution.

Chlorine vapors were detected throughout the course of the reactions, which was managed by closing the reaction vessels with their screw tops and then inverting and up-righting the vessels three times, prior to testing the reaction vapors with moistened KI paper. Since the oxidation of chloride drove the room temperature reactions to reduce potassium permanganate under acidic conditions, it seemed necessary to test reaction progression by presence of chlorine vapors. The time to reaction completion was based on cessation of chlorine emission according to the purple colorization of moistened KI paper. Although time to product precipitation was determined to be complete within 2 h by evidence of clarified supernatant above the dark brown precipitate, chlorine emission continued into the fourth day of wet-aging of the precipitated Mn-oxides in the mother liquor for the reproduced reactions. Due to chlorine gas emission from strongly exothermic reactions, the reactions were performed in a fume hood.

Each reaction product was aged overnight at room temperature, tested for chlorine emission, and then subsequently wet-aged in the mother liquor an additional 48 h at room temperature for the reported samples. The products of the reactions were centrifuge-washed at 2,800 rpm (dial) using 18 MΩ/cm NANOpure® H_2O until the conductivity of

the washes did not exceed 0.14 mS (digital meter). This technique of washing is a common technique used to wash nanomaterial Mn-oxides; since filter paper leads to loss of product, (the material is lost through the pores of the filter paper). Then the products were vacuum-dried and stored in polyethylene screw top bottles at room temperature until sample analysis. The percent yield determined with common gravimetric calculations for product yield, which is outline by Equation 4, where actual yield is the mass of the product and theoretical yield is calculated from the balanced reaction (Eqn. 5). The mass of expected product (MnO_2) is calculated from original grams used of $KMnO_4$. The relationship between MnO_2 and K MnO_4 is taken as 1:1.

$$\%Yield = \frac{actual\,yield}{theoretical\,yield} x100 \quad (4)$$

$$2\ MnO_4^- + 6\ Cl^- + 8\ H^+ \rightarrow 2\ MnO_2 + 3\ Cl_2 + 4\ H_2O \quad (5)$$

Several solid state techniques were used in this study for product characterization, which included BET, SEM, EDS, XRD, and TEM. The analyses of samples were used to correlate the results with the apparent parameter of influence. The reactions produced nanostructured Mn-oxide mineral phases of Birnessite (δ-MnO_2) and Cryptomelane (γ-MnO_2).

3.2 Nitrogen Adsorption

Nitrogen adsorption (BET method) at an isotherm condition of 77 Kelvin was used to measure the specific surface area of samples using the Gemini® 2370 (Micromeritics®). A standard reference material (SRM) Kaolinite (lot no. 19672-18 Micromeritics, with a specific surface area of 15.9 m^2g^{-1}) was used as a performance check of the instrument. Prior to analysis samples were dried and degassed, under nitrogen at 180 ^oC for 24 hours,

using the Flow Prep® 060 (Micromeritics). Specific surface area was calculated as measured surface area relative to sample mass (m^2g^{-1}) using the Brunauer-Emmett-Teller (BET) method. BET was named after the theorists that proposed this method for measuring surface areas of powder samples [49]. The method uses a 4-point measurement at normalized values of pressure with p/p^0 = 0.08, 0.2, 0.3, and 0.4.

3.3 Scanning Electron Microscopy and Energy Dispersive Spectroscopy

The JEOL® JSM-5610 was used for Scanning Electron Microscopy (SEM) and Energy Dispersive Spectroscopy (EDS). Microscale topography was observed with SEM for which the instrument was operated at 15 kV accelerating voltage using secondary electron imaging (SEI) studies using the SEI detector. SEM secondary electron imaging explores physical characteristics of the surface of material to a depth of 10's to 100's nm, which are produced by some elemental arrangement that gets translated throughout the surface of the sample. The apparent highs and lows of SEM topography are produced by sample surface roughness along with take-off angle of the electrons relative to the detector. Characteristics of the material's surface that allow electrons to pass or to be repulsed strongly (the gold may not get into all surface irregularities and subsequently the areas with out the gold coat will be nonconductive for Mn-oxide samples) and the overall surface roughness will influence the appearance of bright and dark regions. The samples were mounted onto aluminum stubs with conductive tape and then gold coated to improve signal detection intensity and hence image resolution.

Semi-quantitative determination of the elemental composition of the samples used a JEOL JSM-5610 SEM operated at 30 kV accelerating voltage with the Oxford Instruments ISIS® EDS. The minimum detection limits for EDS are approximately 0.1 to

a few atom percent. EDS is a chemical microanalysis technique. Electrons are ejected from surface atoms. Electrons from a higher state fill the vacancies and the energy difference is balanced by emission of an x-ray (the energy of which is characteristic of the element). These x-rays get detected and measured against a reference database, which allows analysis of the element composition. The x-ray spectrum energy versus counts is used to determine the elemental composition. Although the Oxford Instrument's ISIS program was utilized, the nature of the ISIS calibration limits the minimum obtainable detection limits of the elements analyzed. Thus, we consider the method, under these circumstances, to be a semi-quantitative method rather than purely quantitative. The main use of the EDS method in this research was to identify the elements in a sample.

3.4 X-ray Diffraction and Refinement of Unit Cell Parameters

The samples were measured using a PANalytical® X'Pert PRO X-ray diffractometer with a multiple-Si-strip solid-state detector (X'Celerator®) at 40 kV and 40 mA operated at 25 ^{o}C and $Cu_{K\alpha 1/2}$ radiation (λ_{ka1} = 1.540596 Å, λ_{ka2} = 1.544493 Å). Synthesized Mn-oxide samples were prepared for X-ray Diffraction (XRD) measurements along with an internal standard (NIST SRM Si640c, a = 5.431195 Å [50]) on a low-background silicon disc. The signal intensities as measured over the sample were recorded using a 0.008° step size per ^{o}2-θ, at a rate of 50 seconds per step size. Observable intensities of a powder-XRD pattern reflect the structural arrangement realized in nanostructured material. Across a powder pattern, a profile function was fitted to the observed intensities using a pseudo-Voight profile algorithm. The refinement parameter of significance in the pseudo-Voight function is the mixing parameter for the peak shapes that characterizes the ratio of Gaussian relative to Lorentzian. The purpose of the profile function [51] was to

obtain peak parameters that described the measured scan. The ICDD (International Center for Diffraction Database) PDF-2 powder diffraction files reference database assisted in the identification of a likely mineral phase match for the samples as well as to gain information about the sample lattice parameters. The fitted profile was then used to compare the sample data with suggested reference data (search matches) from the ICDD PDF-2. Once a reference phase was identified, this phase was converted into a profile phase, and subsequently the sample lattice parameters were calculated based on this converted phase profile. Reference ICDD data often corresponds to reference mineral phase data in the Inorganic Crystal Structure Database (ICSD) database, which contains crystal structure data. Results from unit cell refinement produce information about indexed lattice planes, d-space, and lattice constants both for raw (observable) measurement as well as for a calculated profile.

The MnO_2 based nanomaterial as synthesized exhibits medium-range ordered (5-20 Å) structural arrangements. In this work, the term “amorphous” will be avoided since it is not selective to describe the real nature of structural properties of MnO_2 based nanomaterials within this thesis. Crystals are considered having long-range structural order (> 20 Å), meaning there is based on symmetry operations defined by the space group, repetition of a characteristic arrangement (motive, asymmetric unit, unit cell) within the internal structure again and again to ranges far above 20 Å. In other words, a perfect crystal as defined by theory is defect free (including surface) and exhibits infinite far-range order. The nanomaterials as synthesized within this context do show structural interruptions with 5 to 20 Å intervals due to high concentration of defects mainly point defects, narrow angle grain boundaries, edge dislocations, and mosaics. In comparison,

the crystal structure of the NIST SRM 640c reference material (silicon powder) is far-range ordered and exhibits defect free structural repetition far beyond 20 Å as well as sharp XRD diffraction peaks with FWHM of 0.1 to 0.2 °2Theta. The XRD pattern of MnO_2 specimen as synthesized are characterized with rather broad diffracted peak intensities in the range of 1 to 2 °2Theta which is expected for medium-range ordered (5-20 Å) nanomaterials. XRD patterns of purely near-range ordered (2-5 Å, "amorphous") samples do not show diffracted intensities, but increased diffracted intensities as Gaussian-type radial distribution functions, which describe average cation-anion bonding distances in the structural building units (e.g. cation-anion relation in SiO_4^{4-} tetrahedral in SiO_2 glass). Actually, structural arrangements in near-range ordered materials (glass) are traditionally characterized by WAXS (Wide-Angle X-Ray Scattering) using synchrotron X-ray emission. Hereby researchers intend to determine the first sharp diffraction peak (FSDP) in order to characterize structural- and chemical- clusters within glasses or glass melts. The XRD patterns of the current study present with peak broadening characteristic of nanomaterial. An example of amorphous material was shown in one of our earlier publications [52] presenting amorphous glass as compared to glass prepared with SRM Si640, in which the diffracted intensities of the glass distinctly possess features of a Gaussian-type radial distribution function.

The practice of crystallography is complicated by the morphology of Mn-oxide nanomaterials [53]. Many of these materials possess lamellar shapes and conform to spherical shape at the bulk level. Spherical morphology presents unique problems for XRD [54]. Therefore, we employed the use of HRTEM studies to confirm mineral phase identifications made with XRD.

3.5 Transmission Electron Microscopy

Transmission Electron Microscopy (TEM) images were obtained using a FEI Tecnai® G^2 F30 Super-Twin TEM system, which operates at 300 kV. The 2-D morphology of each sample was explored using transmission electron microscope in bright field mode (BF). Characterization of materials at resolution down to atomic scale (point-to-point resolution of 0.2 nm) can be achieved with the use of an energy filter in high resolution mode (HR) with this electron microscope. The structure phase of the synthesized Mn-oxide samples was explored using high-resolution electron microscopy (HRTEM). Preparation for BFTEM/HRTEM analysis was done using 5-minutes of sonication in a Branson® 2200 sonicator in which 3 mg of sample was suspended in a glass beaker (previously washed with nitric acid) containing 10 mL of 2-propanol. Two drops of the resulting solution matrix were added to a holey-carbon-coated support grid (Ted Pella®, Inc. #01800-F), which was then viewed with a Zeiss® optical light microscope to determine evidence of particles of the sample present on the grid. Each grid, which was prepared with sample, was then dried in a desiccator for one-hour prior to exposure to the high vacuum of the TEM to protect the internal chambers of the instrument. To verify the lattice fringe, Fast Fourier transform (FFT) data of the region of interest (ROI) were measured using Digital Micrograph® software. The FFT of the real image provides evidence of lattice fringe, which arises due to phase interference (contrast) caused by repeat lattice planes [[55]]. Thus, as we correlate indexed repeat lattice planes with their measured d-spacing, so too we correlate measured planes (indexed repeat planes) with the evidence of planes (lattice fringe d-space) [[56]].

CHAPTER 4

RESULTS

In the current study, Mn-oxide polymorphs (Birnessite and Cryptomelane) were precipitated from solution by reduction of potassium permanganate under acidic conditions at room temperature followed by aging in the mother liquor. The underlying influence is unknown as to which parameter influences formation of layer- or tunnel-structure type Mn-oxide mineral phases. This research contributes to current knowledge in the field of Mn-oxide [57,58,59,60].

Table 1. The procedures used to produce the samples in this research are denoted V1P76A, V1P76B, V1P77C, and V1P78D.

Procedure	$KMnO_4$	NaCl	KCl	HCl	H_2SO_4	T	Wet-Age Time
V1P76A	0.125	----	----	0.500	----	16	72 h
V1P76B	0.125	3.00	----	0.500	----	16	72 h
V1P77C	0.125	----	3.00	0.500	----	16	72 h
V1P78D	0.125	3.00	----	----	0.500	16	72 h

* The units of chemical concentration (M) are in terms of molarity and the units of temperature (T) are Celsius.

Reaction parameters were varied, which included chloride, sulfate, sodium, and potassium. More specifically, the parameters of this research included concentrated alkali

chloride salt (as NaCl, KCl) for variation of the counter-cation (Na^+ vs. K^+) to the halide (Cl^-) as well as variation of reagent acid counter-anion (Cl^- vs. HSO_4^-) of acids HCl and H_2SO_4, respectively. The samples produced in this research are pure-phase Mn-based oxide products known by the mineral names Cryptomelane and Birnessite. The products were characterized by BET, SEM, EDS, XRD, and TEM for specific surface area, imaging of topography and microstructure analysis, qualitative elemental analysis, identification of mineralogical phase, morphology, imaging of nano-structure and mineral phase confirmation. Information about the described synthesis procedures of samples (in brief terms) is collected in Table 2. Information about the samples, as gained from BET and XRD measurements as well as percent yield for the reactions, is presented in Table 3.

Table 2. Information about the samples, as gained from BET and XRD measurements as well as percent yield for the reactions is presented in the table. The samples include V1P76A, V1P76B, V1P77C, and V1P78D.

Sample	BET Surface Area [m^2g^{-1}]	ICDD PDF-2	Reference ICSD	Mineral Phase	Chemical Formula	% Yield
V1P76A	24.2	87-1497	83236	Birnessite	$K_{0.5}Mn_2O_{4.3}\cdot 0.5H_2O$	93.6
V1P76B	25.1	87-1497	83236	Birnessite	$Na_{.34}K_{0.16}Mn_2O_{4.3}\cdot 0.5H_2O$	95.4
V1P77C	24.0	87-1497	83236	Birnessite	$K_{0.5}Mn_2O_{4.3}\cdot 0.5H_2O$	95.3
V1P78D	335	77-1796	59159	Cryptomelane	$K_{1.33}Mn_8O_{16}$	95.8

4.1 General Description of Product Synthesis

The reaction involving concentrated KCl was an observably more vigorous exothermic reaction than the reaction involving concentrated NaCl. However, both reactions occurred with an immediate outpouring of opaque and noxious clouds of Cl_2. The solution coloration for the reaction for V1P77C was pink-red. The solution coloration for the reaction for V1P76B was pink-red. Total reaction time to precipitation was 2 hours. At 2 h, the supernatants of both reactions were clear and colorless. The products were wet-aged for a total of 3 d in the mother liquor during which emission of Cl_2 gas continued. At 48 h of cold wet-age time, the supernatants were clear and colorless above the settled dark brown precipitates. The products were then washed and vacuum dried. The final dried product appeared to be powdery textured, solid particles. The coloration of the V1P77C was reddish brown whereas for V1P76B the coloration was dark brown without reddish tint. The percent yield for the product V1P76A was 93.6 %. For the product V1P76B, the percent yield was 95.4 %. The percent yield for the product V1P77C was 95.3 %. For the product V1P78D, the percent yield was 95.8 %. All reactions were exothermic, which resulted in reaction mixtures to increase in temperature as qualitatively evidenced by the rapid increase in warmth of the reaction vessels. Specific temperatures should be measured under calibrated and uniform conditions, which will obtain precise temperature measurements without the possible inconsistencies of hand-measuring with a standard thermometer. This will be done in additional studies. It may be prudent at this juncture to simply identify that the reaction vessels were warm to the touch and that the exothermic nature of these reactions could be visually identified (qualitatively) by the bubbling of the solutions and voluminous exodus of chlorine gas all

occurring within seconds of reactant mixing. The justification for this method is that we were in the process of initial development of these techniques and were interested at the time in measurement of the products. Quantitative measurements during the reactions require specialized instrumentation, which unfortunately was not available to us at the time of development of the current study.

4.2 Nitrogen Adsorptive Isotherm

Specific surface area as measured with BET, for the sample V1P76A, was 24 m^2g^{-1}. For the sample V1P76B, the value of the specific surface area was 25 m^2g^{-1}. For the sample V1P77C, the value of the surface area was 24 m^2g^{-1}. Conversely, for the sample V1P78D the specific surface area measured 335 m^2g^{-1}, which is high for this class of materials [61].

The BET analysis suggests that the specific surface area difference is little influenced for the reactions V1P76A, V1P76B, and V1P77C, which were close to measurements made of biogenic Mn-oxides produced by Toner, et al. [62]. However, for the reaction V1P78D there was profound influence on the specific surface area. Our previously reported [63] SA of 150 m^2g^{-1} for Cryptomelane that was produced using manganous sulfate (e.g. $MnSO_4$), acetic acid, potassium permanganate and applied temperature (similar to the method of McKenzie, 1971). Additionally, Cryptomelane has been reported with SA as high as 222 m^2g^{-1} as reported by R. M. McKenzie (1971), which was produced from the reduction of potassium permanganate by $MnSO_4$ in the presence of acetic acid.

4.3 Scanning Electron Microscopy and Energy Dispersive Spectroscopy

The SEM images were obtained at 15 kV accelerating voltage using secondary electron imaging. EDS was obtained at 30 kV accelerating voltage using backscattered electrons. Elemental composition of the samples used a JEOL JSM-5610 SEM operated at 30 kV accelerating voltage with the Oxford Instruments ISIS® EDS. The minimum detection limits for EDS are approximately 0.1 to a few atom percent.

SEM for the sample V1P76A as presented in Figure 1 (a and b) suggests the spherical units are apparently 250-300nm.

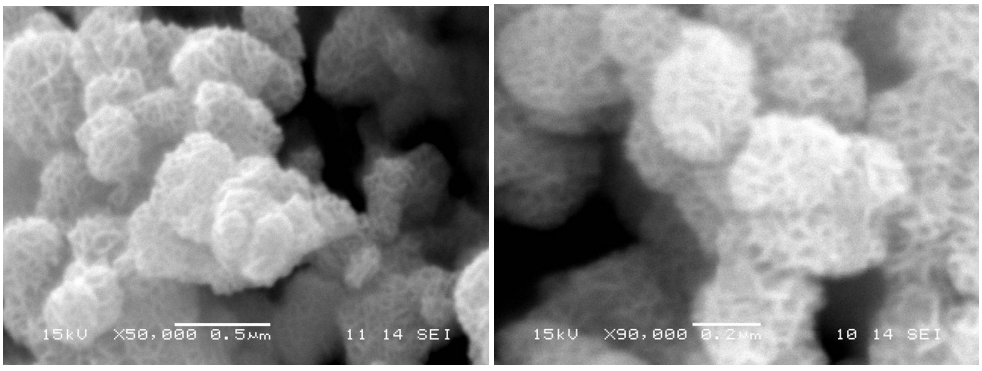

Figure 1. SEM images of the sample V1P76A at (a) 50,000X magnification and (b) 90,000X magnification.

Somewhat similar micro-morphology as that of the sample V1P76A is observable in the SEM image for the sample V1P76B [Figure 2]. As shown in Figure 2 (a and b) of the sample V1P76B, the particles appear to have corrugated topography with partially segregated lobules that have developed into systems larger than 200 nm, but smaller than 500 nm.

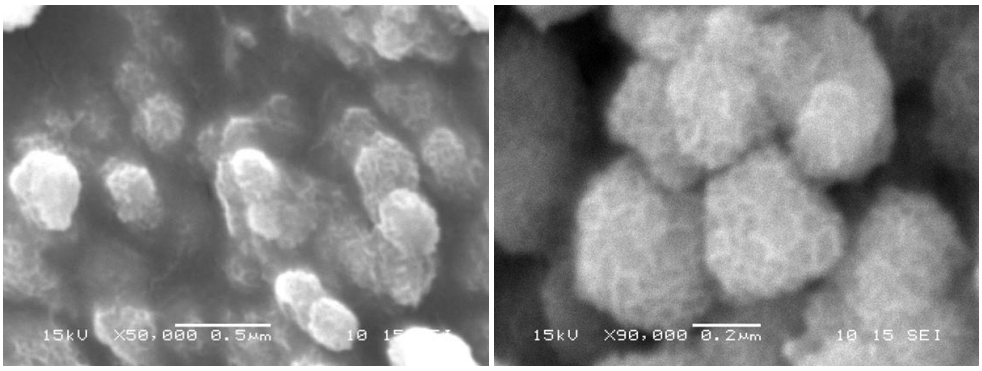

Figure 2. SEM images presenting the sample V1P76B at (a) 50,000X magnification and (b) 90,000X magnification.

As viewed in the SEM image of sample V1P76B, shown in Figure 2, the apparent surface features, which were produced by secondary electron scattering, may appear to present with a texture gradient suggestive of physical depth of ~500 nm. Conversely, these qualities of linear perspective may not render a similar illusion at 90 kX magnification for the sample V1P76B. The particles of sample V1P76B appear to be larger than 200 nm, but smaller than ~500 nm, although the scale bar in comparison with visible particles suggests that the lobule sizes measure less than ~500 nm.

The SEM images for the sample V1P77C, as shown in Figure 3 (a and b), present corrugated lobules that appear to be larger than 200 nm. However, some of the lobules appear to be agglomerated into larger growths, still lacking uniformity of size, but being of approximate sizes greater than 500 nm. The lobules comprising the overall sample of V1P77C appear of similar development as the samples V1P76A and V1P76B. The SEM scale indicates that the lobule sizes comprising the overall topography of both samples, V1P76A and V1P76B, measure less than 500 nm.

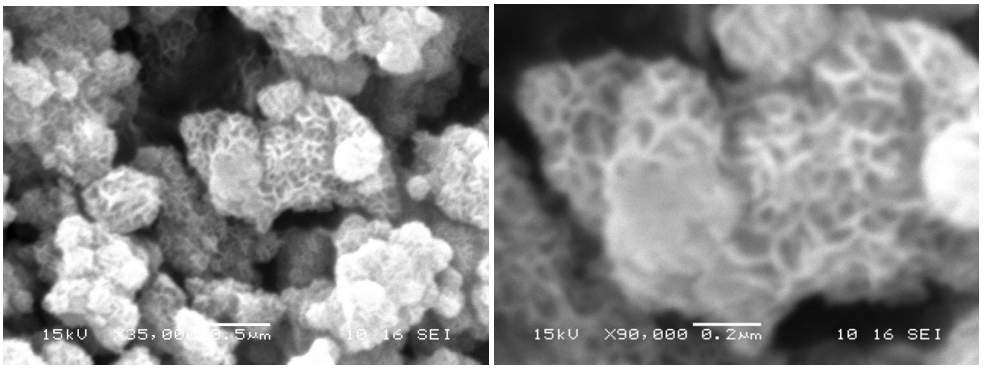

Figure 3. SEM images of the sample V1P77C at (a) 35,000X magnification; and (b) 90,000X magnification.

As shown in Figure 4 (a and b) interesting topography is presented in the SEM image for the sample V1P78D. There are apparent needle-like projections from a central internal region of each independent spherical mass, which gives the spheres an appearance of spiny sea urchins. The SEM images of V1P78D suggest the particles appear to be larger than 250 nm, but smaller than 550 nm, on average, the particle diameters appear to be on the order of approximately 0.5 um (500 nm).

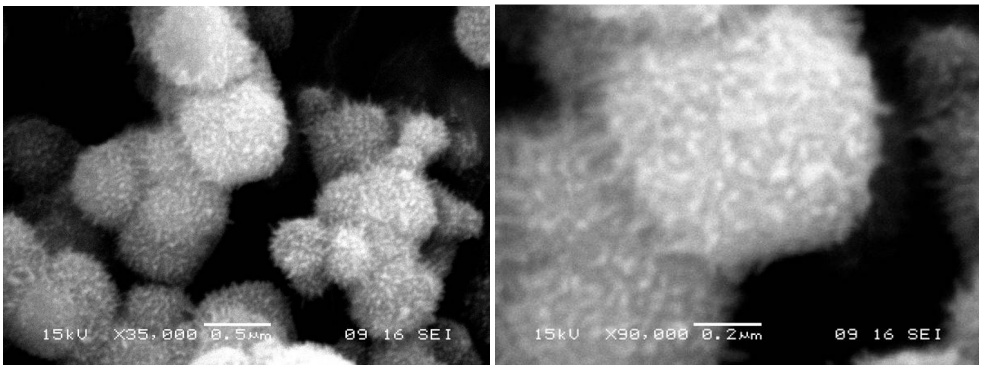

Figure 4. SEM images for the sample V1P78D obtained at magnifications of 35 kX (left) and 90 kX (right).

SEM alone can not accurately describe the physical characteristics of these samples. This is due to the nature of SEM secondary electron imaging which indicates physical characteristics of the surface and near surface of material to a depth of 10's to 100's nm produced by some elemental arrangement that gets translated throughout the surface of the sample. For instance in the samples V1P76A, V1P76B, and V1P77C the SEM SEI images presented with lobules produced by irregular patterns of bright (high Z-mass) lines interrupted by dark (low Z-mass) patches giving the impression of corrugated matter. Conversely, the sample V1P78D presented with bright spots and streaks with evidence of spiny protrusions whereas samples V1P76A, V1P76B, and V1P77C presented with surface features that appeared corrugated.

EDS is a well-known chemical microanalysis technique. The minimum detection limits for EDS are approximately 0.1 to a few atom percent. Electrons are ejected from surface atoms. Electrons from a higher state fill the vacancies and the energy difference is balanced by emission of an x-ray (the energy of which is characteristic of the element).

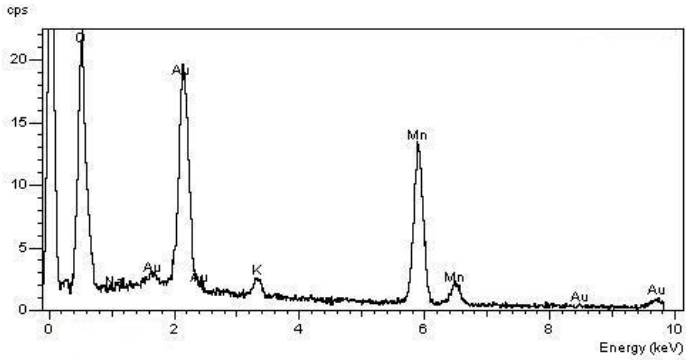

Figure 5. EDS spectrum for the sample V1P76A identified elements potassium, manganese, and oxygen.

As shown in Figure 5, elements present in the sample V1P76A were identified with EDS as potassium, manganese, and oxygen. As measured with EDS, as shown in Figure 6, elements present in the sample V1P76B were identified as sodium, potassium, manganese, and oxygen. As measured with EDS, as shown in Figure 7, elements present in the sample V1P77C were identified as potassium, manganese, and oxygen.

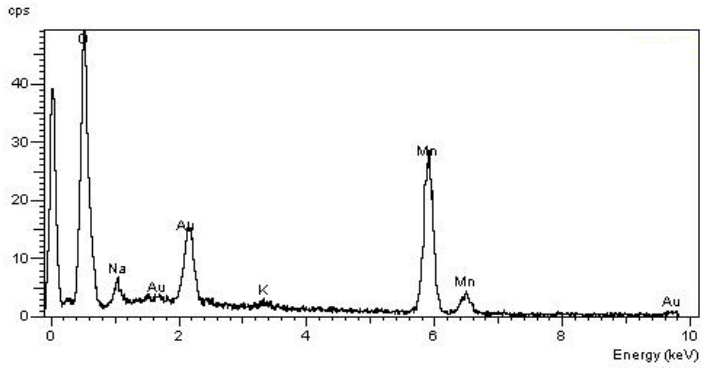

Figure 6. EDS spectrum for the sample V1P76B identified elements sodium, potassium, manganese, and oxygen.

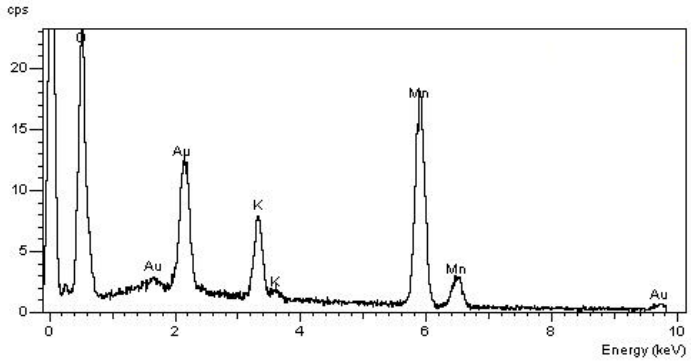

Figure 7. EDS spectrum for the sample V1P77C identified elements potassium, manganese, and oxygen.

The presence of Au in the EDS spectra of the measured samples was due to the process of gold sputter-coating the samples prior to EDS analysis. In the EDS of V1P76B [Fig. 6], the presence of Na, Mn, and O are suggested, whereas for V1P77C [Fig. 7] the presence of K, Mn, and O are suggested. An approximate K:Mn ratio for the sample V1P77C suggested 1:2.5; and for the sample V1P76B, an approximate Na:K:Mn ratio appeared to be 1:2:12. It is interesting that the total alkali cation to manganese ratio as measured with EDS for the sample V1P76B was 3:12 (1:4), whereas for the sample V1P77C the ratio was 1:2.5. This corresponds to about 38% higher proportion of alkali cation incorporation into the sample V1P77C. The EDS for sample V1P77C [Fig. 7] suggested more then twice the potassium counts per second (semi-quantitative method) as that for the EDS of sample V1P76A [Fig. 5]. An approximate K:Mn ratio for the sample V1P77C suggested 1:2.5; an approximate K:Mn ratio for the sample V1P76A suggested 1:5. It is interesting that the potassium is elevated for V1P77C relative to V1P76A, which can not be related to the wet-aging time, as all samples were wet-aged in the mother liquor for the same duration. However, there was a different composition between reaction matrices for the reactions that produced sample V1P76A (no 3.0 M KCl salt dissolved into potassium permanganate solution prior to HCl addition) and sample V1P77C (3.0 M KCl salt dissolved into potassium permanganate solution prior to HCl addition). This result suggested increased incorporation of reaction cations into the final Birnessite product during sample formation of V1P77C, which is consistent with studies that indicate Birnessite strongly sorbs and exchanges cations [[35-38]] under acidic conditions.

EDS for the sample V1P78D, as shown in Figure 8, suggest the presence of K, Mn, and O. Element identification using EDS indicated sulfur was not present in the V1P78D sample [Fig. 8], which was produced in the presence of sulfate, which correlated well with data we produced in previous studies ([64]) of cryptomelane synthesis as a double decomposition reaction using solid potassium permanganate and Ultrex concentrated sulfuric acid.

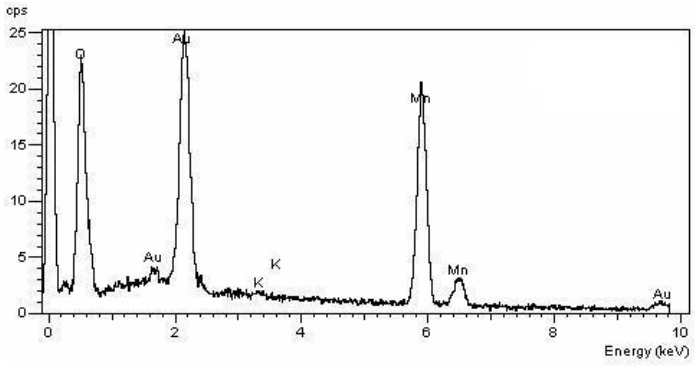

Figure 8. EDS spectrum for the sample V1P78D identified elements potassium, manganese, and oxygen.

The EDS for sample V1P78D [Fig. 8] suggested the presence of K, Mn, and O, whereas for the sample V1P76B [Fig. 6] EDS suggested the presence of Na, K, Mn, and O, for reactions in which only the type of acid used, and hence, the presence of sulfate was realized in reaction V1P78D as the parameter change. That the EDS did not detect sodium present in the sample V1P78D is curious, as a significant amount of sodium was present in both reaction matrices that produced sample V1P76B and sample V1P78D. Since the presence of sulfate is the only parameter variation between these two reactions, this result indicates that there is some interference or influence produced by the sulfate

species, which deterred the adsorption of the sodium cation from the reaction matrix and subsequent incorporation into the sample V1P78D.

4.4 X-ray Diffraction and Unit Cell Parameters

The XRD patterns for the samples suggested material with distinctive medium-range order across the region of sample being measured, which is consistent with nano-sized Mn-oxides. TEM studies were used to confirm the indexed planes and corresponding d-spacings, which will determine if the mineral phase as measured with XRD was correctly identified.

The XRD pattern presented in Figure 9 is for the sample V1P76A, which was measured using Highscore Plus software to obtain the lattice parameters. The relative line intensities were compared to ICDD PDF2 to find a crystal phase match, which was found to be comparable to reference pattern 87-1497 (reference ICSD 83236). The reference phase corresponds to mineral phase Birnessite of a specific sub-type, which is a K-Mn-oxide-hydrate, also known as a potassium-rich Birnessite [65] (K-Bi). The unit cell of reference ICSD 83236 (Birnessite) crystallizes in a monoclinic space group C12/m1, with a chemical formula of $K_{0.5}Mn_2O_{4.3} \cdot 0.5H_2O$. The unit cell parameters were identified after refinement. Based on the measured XRD relative line intensities and comparison with the ICDD PDF2 identified phase, the lattice parameters for V1P76A were identified. The suggested side lengths of the unit cell were a = 10.0(1) Å, b = 2.813(1) Å, c = 7.73(3) Å, with an angle $\beta = 67.35(9)^{o}$ and a cell volume of 201.5(8) $Å^3$. The diffraction peaks corresponded to d(hkl)-spacings of 7.1(8), 3.5(6), 2.4(3), and 1.4(0) Å. The lattice planes corresponding to these d-spacings were (001), (002), (110), and (310), respectively.

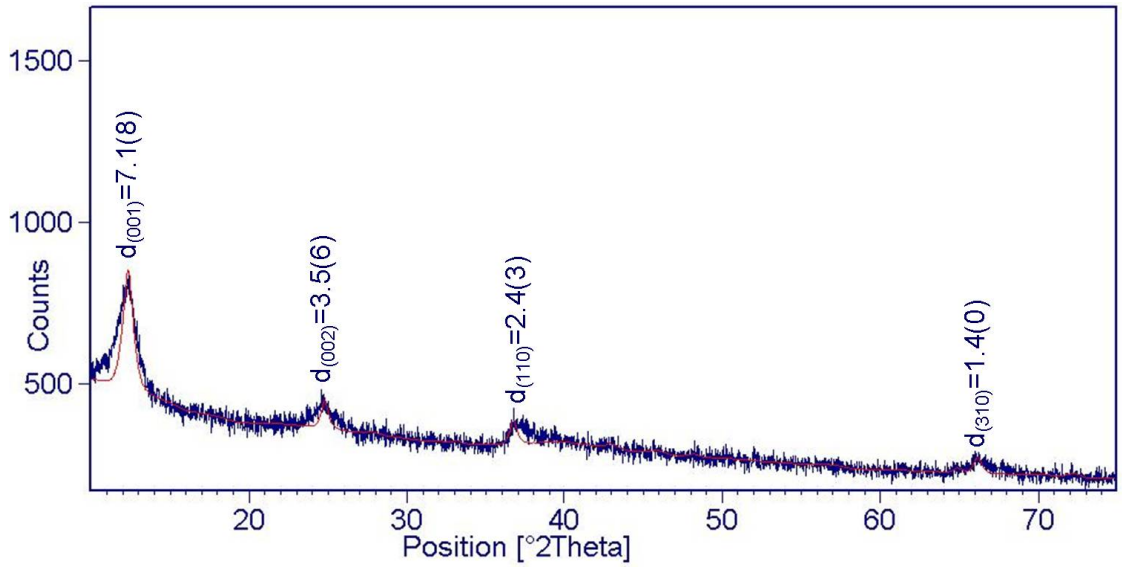

Figure 9. XRD pattern of sample V1P76A was found to be comparable to the mineral phase Birnessite of reference ICSD 83236 with the chemical formula $K_{0.5}Mn_2O_{4.3}$ $\cdot 0.5H_2O$. Final observed (blue scan line) and calculated (red scan line) of XRD pattern.

Subsequently, for the sample V1P76B as presented in the XRD pattern of Figure 10, Highscore Plus software calculated lattice parameters profiled using ICDD PDF-2 #87-1497, which corresponds to reference ICSD 83236. Reference ICSD 83236 is a potassium-bearing Birnessite mineral phase with the chemical formula $K_{0.5}Mn_2O_{4.3}$ $\cdot 0.5H_2O$ that crystallizes in a monoclinic space group C12/m1 (S.G. 12). The side lengths of the calculated lattice parameters were a = 5.041(29), b = 2.827(17), c = 7.664(16); with angle $\alpha = \gamma = 90^{o}$, $\beta = 98.06(51)^{o}$, and a unit cell volume of 108.14(95) $Å^3$. The indexed diffraction peaks corresponded to d(hkl)-spacings of 7.4(7), 3.6(9), 2.4(1), and 1.4(0) Å. The lattice planes corresponding to these d-spacings were (001), (002), (110), and (310), respectively.

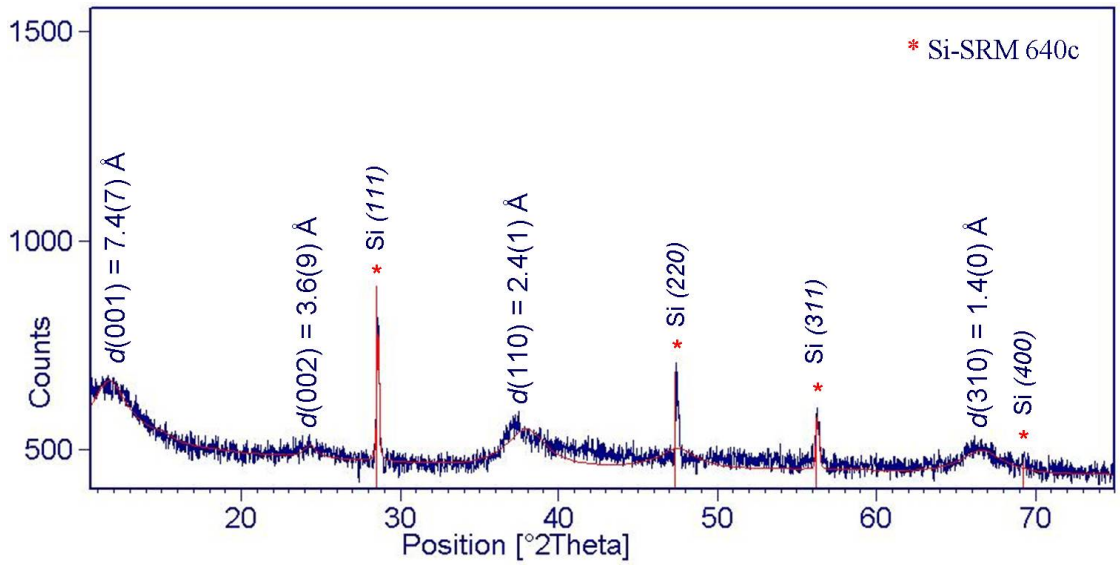

Figure 10. XRD pattern of sample V1P76B was found to be comparable to the mineral phase Birnessite of reference ICSD 83236, which possesses the chemical formula $K_{0.5}Mn_2O_{4.3} \cdot 0.5H_2O$. Final observed (blue scan line) and calculated (red scan line) of the XRD pattern.

Considering the element ratio of 1:2 for K:Na as measured with EDS for sample V1P76B along with overall manganese oxidation state of Mn(3.74), according to XANES determination as measured by Iraida Demchenko et l. [66] for a sample similarly prepared, the chemical formula for our sample might be more like $K_{0.16}\ Na_{0.34}\ Mn_2O_{4.3} \cdot 0.5H_2O$.

Using Highscore Plus software, the calculated lattice parameters of the sample V1P77C, as presented in the XRD pattern of Figure 11, were profiled with respect to ICDD PDF-2 code 87-1497, which corresponds to reference ICSD 83236. The reference phase corresponds to mineral phase Birnessite of a specific sub-type referred to as potassium Birnessite (K-Bi), for which the mineral phase and crystal structure was previously characterized with XRD [67].The unit cell of reference ICSD 83236

(Birnessite) crystallizes in a monoclinic space group C12/m1, with a chemical formula of $K_{0.5}Mn_2O_{4.3} \cdot 0.5H_2O$.

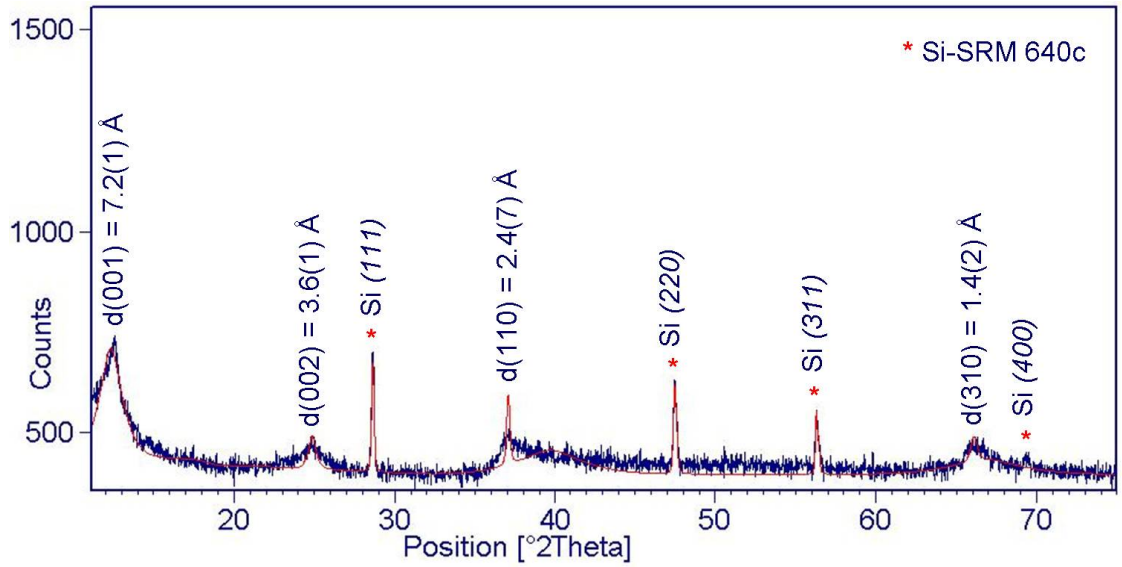

Figure 11. XRD pattern of sample V1P77C was found to be comparable to the mineral phase Birnessite of reference ICSD 83236 with the chemical formula $K_{0.5}Mn_2O_{4.3} \cdot 0.5H_2O$. Final observed (blue scan line) and calculated (red scan line) of XRD pattern.

The side lengths of the calculated lattice parameters were a = 5.05(2) Å, b = 2.855(5) Å, c = 7.27(3) Å, with an angle $\beta = 102.77^{o}$ and a cell volume of 102.77 $Å^3$. The indexed diffraction peaks corresponded to dhkl-spacings of 7.2(1), 3.6(1), 2.4(7), 1.9(4), 1.5(6), and 1.4(2) Å. The lattice planes corresponding to these d-spacings were (001), (002), (110), and (310), respectively.

For sample V1P78D, the XRD pattern shown in Figure 12 is suggestive of a medium-range ordered material. This nature is suggested by the broadened peaks, which is a common finding in XRD patterns for nanomaterial.

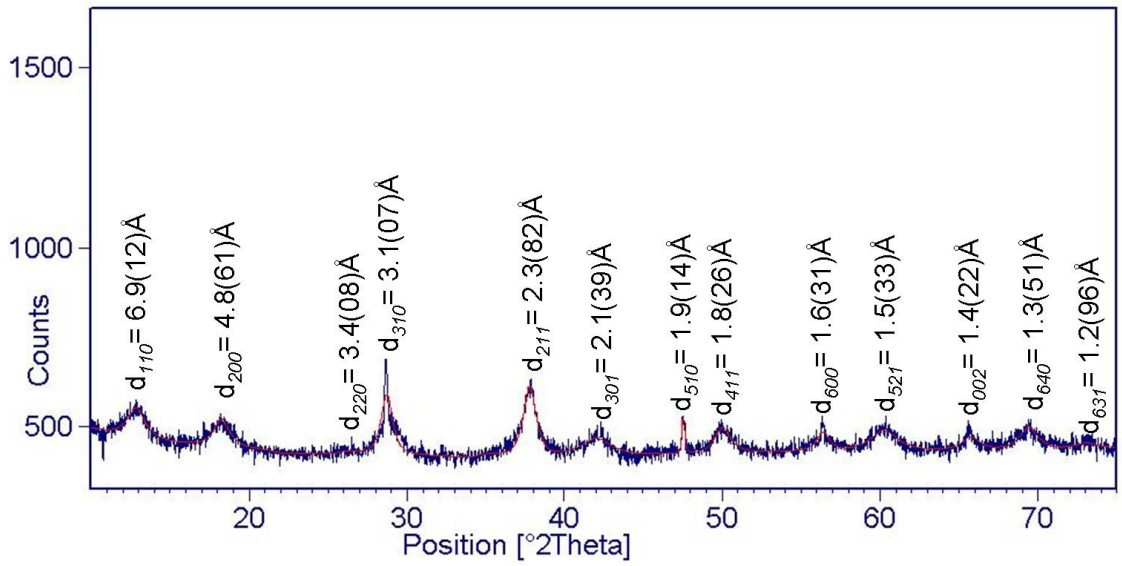

Figure 12. XRD pattern of sample V1P78D was found to be comparable to the mineral phase Cryptomelane of reference ICSD 59159 with the chemical formula $K_{1.33}Mn_8O_{16}$. Final observed (blue scan line) and calculated (red scan line) of XRD pattern.

Using Highscore Plus software for sample V1P78D, the calculated lattice parameters with respect to ICDD PDF-2 code 77-1496 were found to have side lengths $a = b = 9.761$ Å, $c = 2.8445$ Å, with angles $\alpha = \beta = \gamma = 90$ °; and a unit cell volume = 271.02 Å^3. The refined diffraction peaks corresponded to d*hkl*-spacings of 6.9(12), 4.8(61), 3.4(08), 3.1(07), 2.3(82), 2.1(39), 1.9(13), 1.8(26), 1.6(31), 1.5(33), 1.4(22), 1.3(51), 1.2(96) Å. The lattice planes corresponding to these d-spacings were (110), (200), (220), (310), (211), (301), (510), (411), (600), (521), (002), (640), and (631), respectively. The ICDD PDF-2 code 77-1796 corresponds to reference [68] ICSD 59159. The reference pattern ICSD 59159 is the mineral phase Cryptomelane. This Cryptomelane crystallizes in a tetragonal space group I4/m with the chemical formula $K_{1.33}Mn_8O_{16}$.

Thus, XRD analysis suggests the sample V1P78D is Cryptomelane. The Cryptomelane mineral oxide crystal structure has been studied previously using powder-XRD [69,70]. The d(*hkl*) and corresponding spacing distance had to be confirmed from HRTEM studies. The XRD patterns for the samples V1P76A, V1P76B, and V1P77C suggests a semi-crystalline character by virtue of lattice planes of minor intensities, which are not fully developed. Additionally, the tailing of the peaks toward the higher angle side of the diffractogram is an asymmetric profile suggestive of a layer structure [71]. The repeat d-spacing distance approximately 7 Å corresponding to the (001) lattice plane is recognized as a hallmark of the Birnessite class of manganese oxides, which has been well characterized by other research scientists [72,73]. This additional information is suggestive that the mineral phase identified as Birnessite for the samples V1P76A, V1P76B, and V1P77C were reasonably identified. The d(*hkl*) and corresponding spacing distance had to be confirmed from TEM studies.

4.5 Transmission Electron Microscopy

The use of TEM studies and powder diffraction techniques as adjunct tools is effective for nanostructure characterization and mineral phase identification. Lattice fringe may be observable in the real image. A selected Region of Interest (ROI) corresponds with a local area of a real image, from which measurements are made using Micrograph software. In this way, the lattice fringe may be measured with this specialized TEM technique and subsequently correlated to XRD measured values according to the methods outline by H. Hofmeister [74] and by Ma et al. [75].

As presented in the BFTEM image of the sample V1P76A, as shown in Figure 13, regions of observable information are indicated with labels. Region A represents the amorphous carbon film that coats the sample support grid.

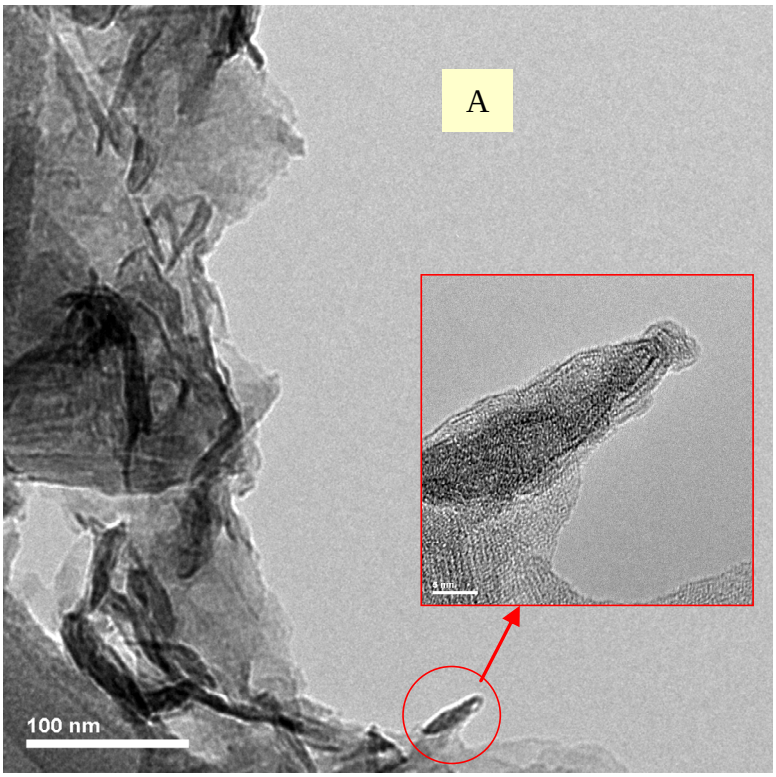

Figure 13. BFTEM image taken at 72kX magnification for the sample V1P76A and 1MX for the encircled region presented (right inset image).

Region B of Figure 13 represents the overall morphology of the sample V1P76A, which suggests material of thin layers with discontinuous morphology comprised of irregular edges along the sample. These irregular edges also appear to be overlapping and deforming in some areas without apparent order or regularity. For Mn-based mineral oxide, thin layer morphologies are produced by layers of manganese oxide octahedral sheets (MOOS). This morphology produced by layers comprised of MOOS may be

described intuitively as presenting with an appearance reminiscent of “flower petals”. The samples, when observed with TEM at various low-to-medium-range magnifications, presented with classically recognized lamellar Mn-oxide morphology. Two encircled regions within Figure 13 were imaged using HRTEM, as presented in Figure 14.

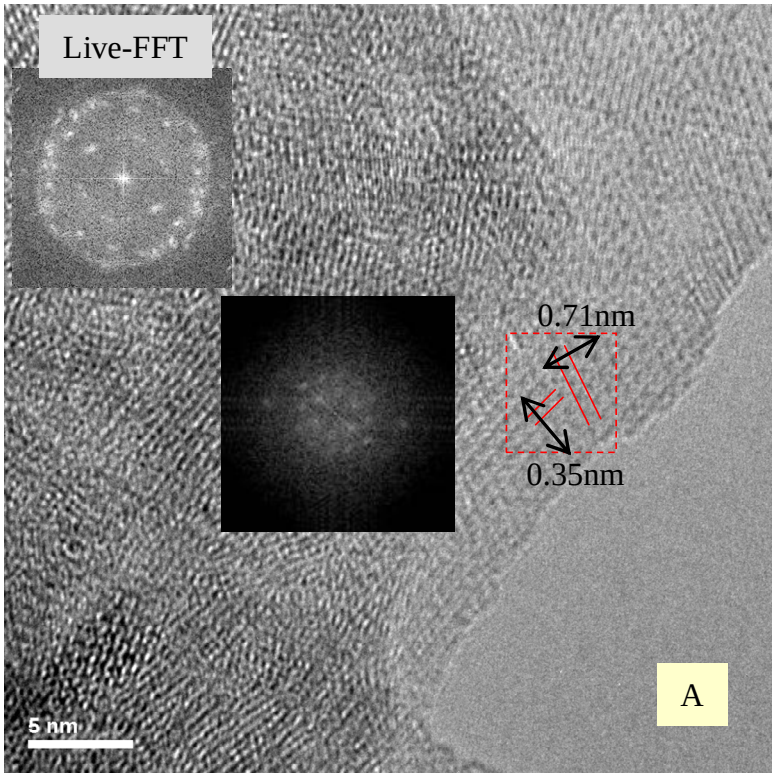

Figure 14. HRTEM image taken at 1MX magnification of the sample V1P76A, which show the major repeat planes of d(001) = 0.71 nm and d(002) = 0.35 nm identified by direct measurement of the real image lattice fringes as well as the corresponding ROI FT micrograph measurements.

For the sample V1P76A, HRTEM suggests [see Figure 14] the major repeat plane of d(001) = 0.71 nm and d(002) = 0.35 nm agreement with XRD measurement. As shown in the right, central region of Figure 14 is the Region of Interest (ROI) in the real image.

The lattice fringes were measured directly from the real image as well as using the Fourier Transform (FT) micrograph in conjunction with Micrograph® software to obtain measured values for the lattice fringe.

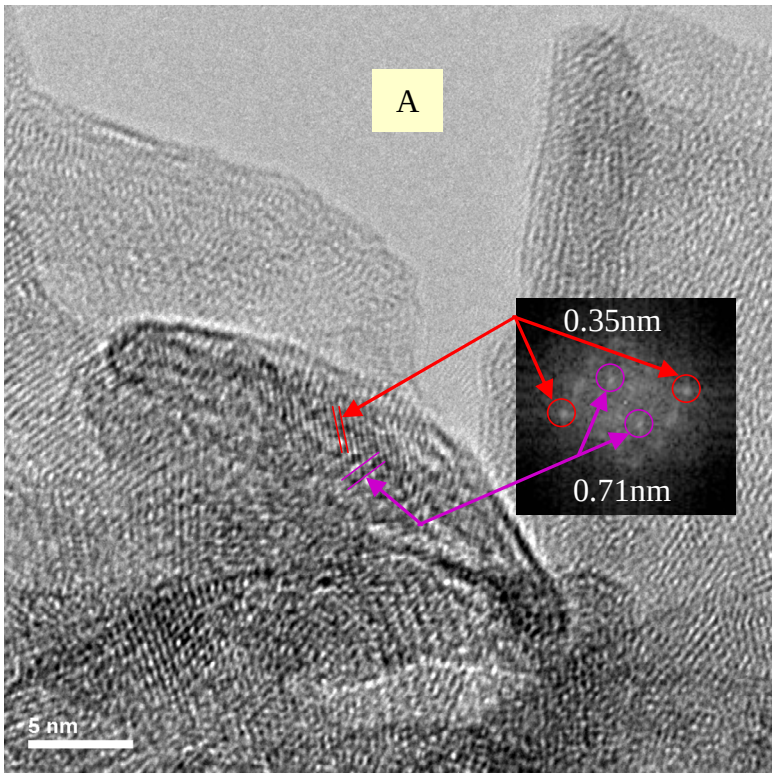

Figure 15. HRTEM image taken at 1MX magnification for the sample V1P76A, which show a ROI FT micrograph along with direct lattice fringe measurements corresponding to 0.71 nm and 0.35 nm, which correlate well with the d(001) and d(002), respectively, as measured with XRD.

For the HRTEM image of Figure 15, Region A represents areas of amorphous carbon film that coats the sample support grid. The FT ROI presents evidence of d-spacing measurements. Indicated are the major plane of interest for the Birnessite phase, which are the d(001) and d(002) indexed planes. In the presented case, lattice fringe d-spaces

were found to measure 0.71 nm and 0.35 nm, which correlate well with the d(001) and d(002), respectively, as measured with XRD. Thus, the combined information gained from XRD and TEM study for the sample V1P76A, which was produced by reduction of 0.125M $KMnO_4$ in solution with 0.50M HCl at room temperature, suggests that the mineral phase that was produced was Birnessite, of reference ICSD 83236.

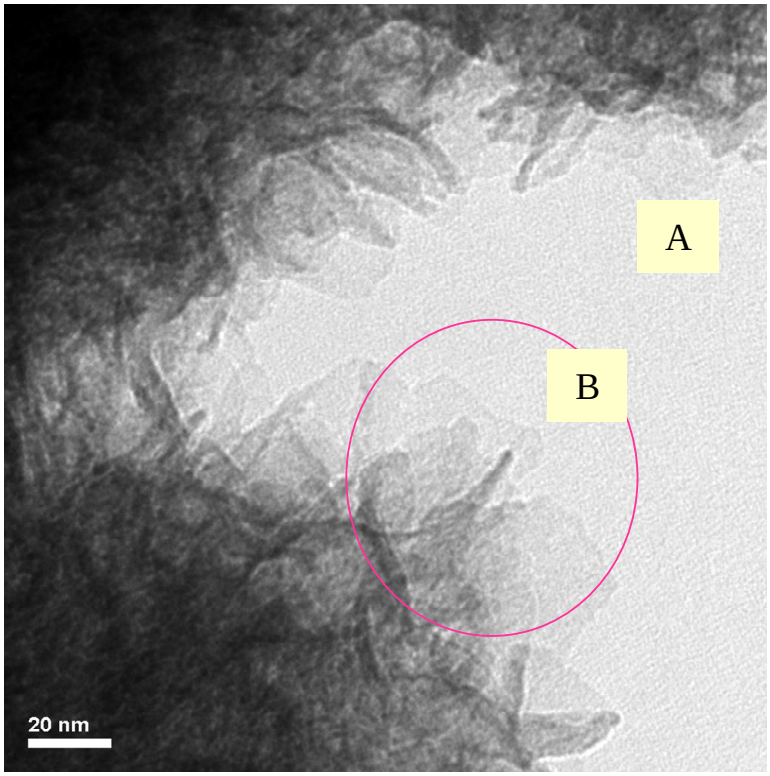

Figure 16. BFTEM image taken at 200,000X magnification for the sample V1P76B, which shows thin layer morphology similar to classic birnessite.

The BFTEM image of the sample V1P76B, as shown in Figure 16, presents with regions of observable morphology information indicated by labels A and B. Region A represents the amorphous carbon film that coats the support grid. Region B represents the morphology of the sample V1P76B observable at multiple sampling positions during the

TEM session. The morphology of sample V1P76B, shown in Figure 16, is suggestive of irregular features comprised of discontinuous thin layers, which appear to thicken or to overlap in some areas without apparent order or pattern. The encircled region of Figure 16 was selected for HRTEM study, as shown in Figure 17.

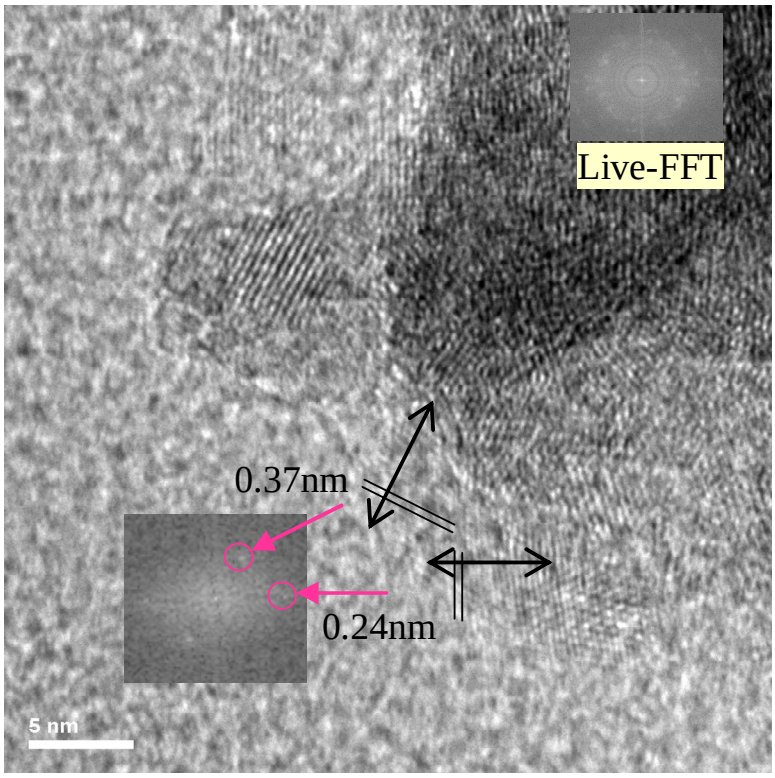

Figure 17. HRTEM image taken at 1MX magnification for the sample V1P76B is presented along with a FT micrograph of the local ROI, which measured 0.37 nm and 0.24 nm correlating with indexed planes for the (010) and (023) as measured with XRD.

In the HRTEM image of the sample V1P76B, as shown in Figure 17, the XRD indexed planes for the (010) and (023) are confirmed by measured lattice fringes and the correlate contrast transform (the local FT) of the local region of interest was selected and measured using Micrograph software, which measured the lattice fringes as 0.37 nm and

0.24 nm, respectively. The FFT is a transform of the “real image” associated with the overall HRTEM image, which in this case shows a hazy region among speckles. This phenomenon of speckles distributed in concentric rings against a hazy background is due to small regions of poly-crystal formed from near-range order arrangement of lattice planes from which the electron beam diffracts. This HRTEM study suggests that the sample V1P76B is nanomaterial, as evidenced by the speckles rather than intense diffraction spots expected of long-range order crystals.

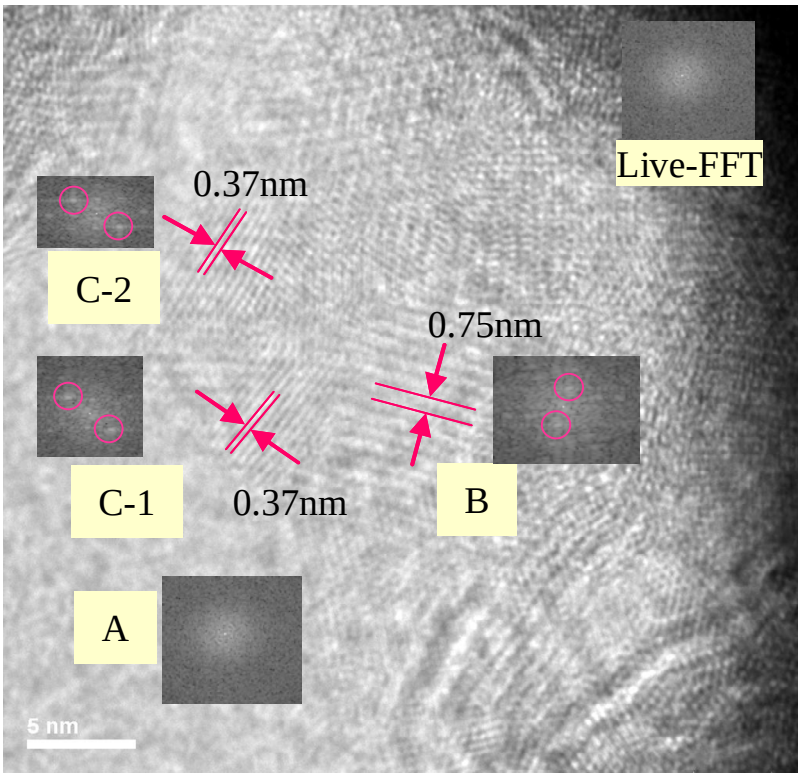

Figure 18. HRTEM image of the sample V1P76B at 1MX magnification is shown with FT micrographs of the local ROI along with direct lattice fringe measurements comparable with lattice d-spacings of 0.37 nm and 0.75 nm, which occur for indexed planes d(010) and d(011), respectively, as measured with XRD.

Figure 18 shows an HRTEM image of the sample V1P76B. Region A of Figure 18 represents amorphous areas produced by the carbon film that coats the sample support grid as confirmed by the local ROI FT micrograph (inset lower left). Region B presented with lattice fringes that measure 0.75 nm, which correlates well with the ROI d-spacing measurements and confirms presence of the d(011) indexed planes as measured with XRD. The measured lattice fringe of regions c-1 and c-2 is 0.37 nm, which correlates well with FT of the ROI lattice fringe spacing measurements subsequently confirming the presence of d(010) indexed planes as measured with XRD. The overall image Live-FFT micrograph is labeled and this contrast image transform is suggestive of polycrystalline or very small grained material. As measured with XRD, for the sample V1P76B, the d(hkl) repeat plane distance for the (010) occurs at 0.37 nm and for the d(011) at 0.75 nm.

Thus, for sample V1P76B, some of the low angle reflections as well as one minor intensity reflection were not well developed. These were confirmed from lattice fringe measurements as seen using HRTEM for d*hkl* of *d*(011), d(010), and *d*(100). The poorly developed XRD d*hkl* reflections were confirmed from TEM studies by observing the presence of d(010) and d(011) reflections using ROI FT micrograph measurements of lattice fringe.

In the BFTEM image of the sample V1P77C, as shown in Figure 19, observable information includes Regions A and B. Region A represents areas of amorphous carbon film, which very thinly coats the sample support grid. Several grid positions were sampled during the TEM session. The overall morphology is represented by Region B, which presents with randomly overlapping thin layers. The encircled regions represent areas of sample imaged with HRTEM magnification.

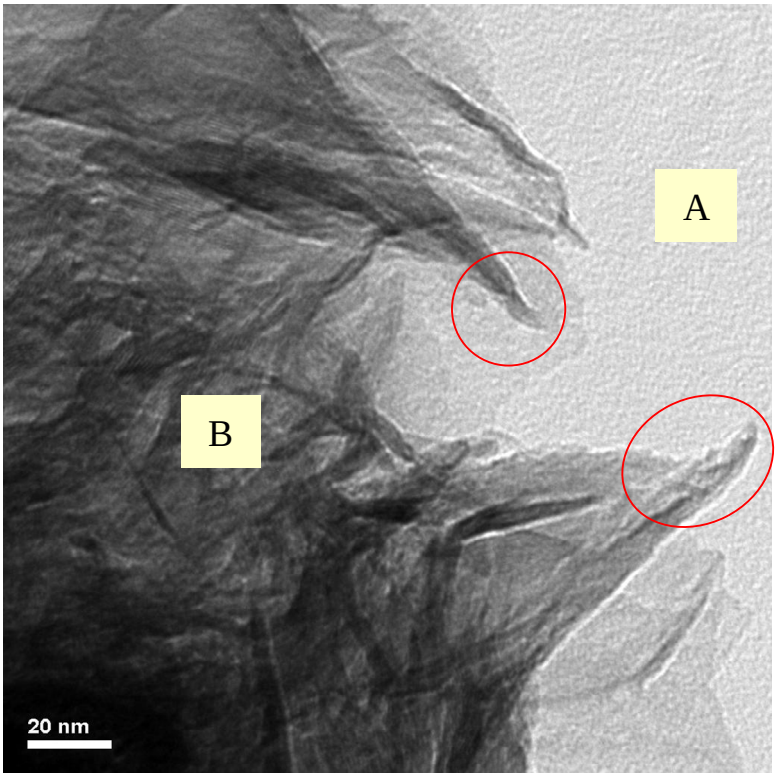

Figure 19. BFTEM image obtained at 200,000X magnification of the sample V1P77C showing morphology comprised of thin layers.

In the HRTEM image of the sample V1P77C, as shown in Figure 20, several regions of interest were investigated as indicated by labels A, B, and C. Region A is representative of the carbon film, which coats the sample support grid. Region B and Region C, which appeared to have “flower petals” morphology when viewed in bright field mode, when viewed with HRTEM these “petals” appear to be crystalline layers of medium-range nanomaterial as suggested by the FT micrograph of the local ROI. The lattice fringes, which are indicated along with the respective transform of the HRTEM “real image”, were found to be 0.72 nm for Region B. The comparisons of the real image

transform and FT of the local ROI is in agreement with the lattice plane intensities as measured with XRD for d(001).

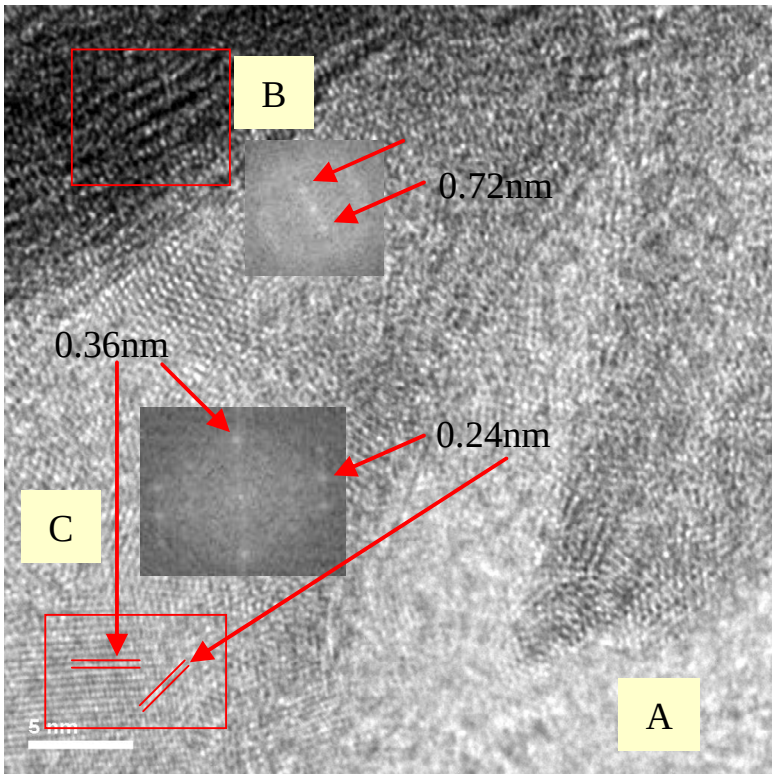

Figure 20. HRTEM image of the sample V1P77C at 1MX magnification, which presents FT of the local ROI that measure 0.72 nm and 0.24 nm confirming the presence of d(001) and d(110), respectively.

For the HRTEM image of the sample V1P77C, as shown in Figure 21, several regions of interest were investigated as indicated by labels A, B, C, and D. Region A is representative of the carbon film, which coats the sample support grid. Region B presented with lattice fringes that measure 0.72 nm. The lattice fringes which are indicated in the transform of the HRTEM "real image" and corresponding FT of the local ROI, confirm the d(001) as measured with XRD, for Region B of Figure 21. The

measured lattice fringe of Region C was found to be 0.24 nm, which correlates well with the ROI d-spacing measurements and confirms the presence of d(110) indexed planes as measured with XRD. Region D lattice fringe spacing and ROI FT were comparable at 0.36 nm which is in agreement with the lattice plane intensities as measured with XRD for d(002). Thus, for the sample V1P77C, the TEM studies confirm the mineral phase - Birnessite for major peak intensities corresponding to d(001), d(110), and d(002), verifying the XRD analysis.

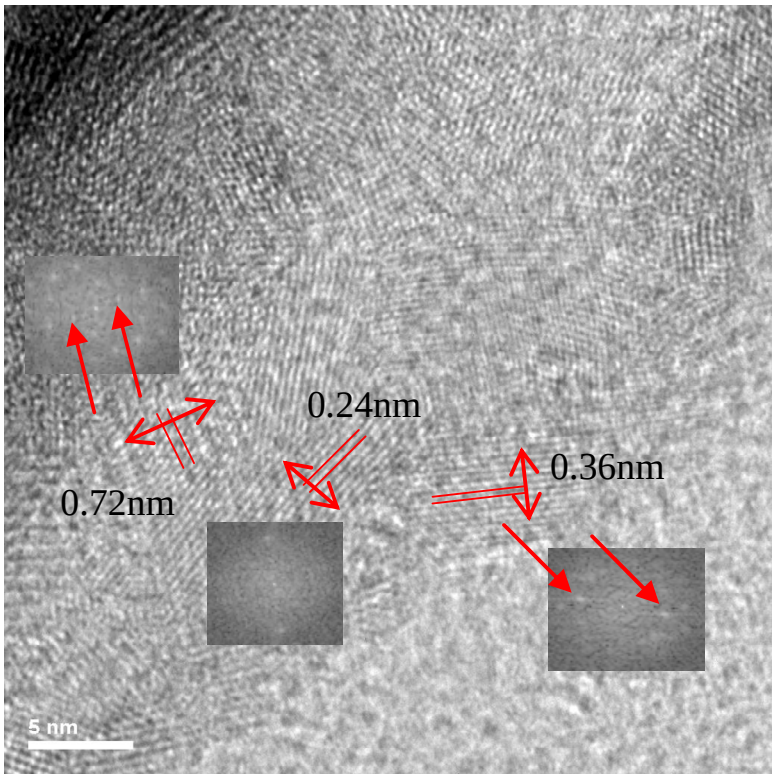

Figure 21. HRTEM images of the sample V1P77C at 1MX magnification of a thin region along the edge of the layer-structure MnO_2.

The BFTEM image of the sample V1P78D, as shown in Figure 22, presents with regions of observable information indicated with labels. Regions A and B comprise the

carbon-coated sample support grid, on which the sample V1P78D is dispersed in random fashion. The sample support grid is comprised of a webbed super-structure (see Region A) of support grid as well as the holes (see Region B) of the grid. The sample support grid is very thinly coated with amorphous carbon film, which produces minimal contrast influence in TEM studies. Region C appears to be comprised of fibrous units of random orientation that are agglomerated into a cluster.

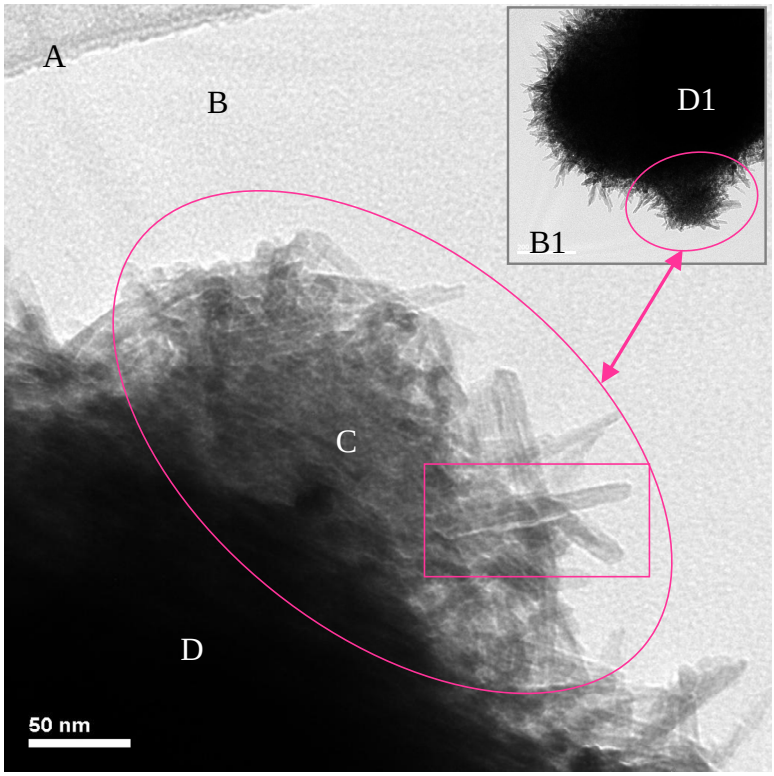

Figure 22. BFTEM image showing clusters of nanorods of the sample V1P78D at 97,000X magnification along with the associate inset image that presents sample V1P78D using BFTEM at 42,000X magnification.

These fibrous units (growths) can not be determined as attached outgrowths from a centralized internal region (the adjacent darker region). The observable fibrous growths

appeared to have lengths of 100 nm and widths of 15-18 nm. Region D shows the darker region adjacent to the clustered fibrous growths, which is not discernable as to whether this region is comprised of amorphous or a region comprised of a greater number of agglomerated fibrous units. The encircled area represents sample that was focused on for HRTEM.

The HRTEM of the sample V1P78D, as shown in Figure 23, presents with regions labeled A, B and C. The HRTEM "real image" was used to generate a Fourier transform of the contrast data for the overall sample presented in the image, which in this case the Live-FFT indicates that the sample of study is in focus and not stigmatic. The live-FFT of the overall "real image" transform is shown in the inset image, which is suggestive of polycrystalline or very small grain material. The transform of the Live-FFT presents as slightly defocused in the z-direction (x,y are not astigmatic as observable by the uniform circumference of the concentric rings). This method of focusing the beam relative to the sample eucentric height using the live-FFT assists in obtaining the image with the x,y direction free of astigmatism. However, there are also bright spots from beam deflection from repeat lattice planes. Region A represents amorphous areas produced by the carbon film that coats the sample support grid as confirmed by the FT. Region B indicated overlap of crystal growths from crystals of random orientation. In the marked ROI at Region C is presented a section of nano-fiber comprising the sample V1P78D in which 0.69 nm and 0.31 nm are lattice fringes that are obtained from direct measurement. Subesequently, the FT of the local ROI at Region C presents with measurements of 0.69 nm, 0.48 nm, 0.31 nm, and 0.21 nm. These d-spacings are consistent with d(hkl) of (110), (200), (310), and (301), respectively, as measured with XRD for the sample V1P78D.

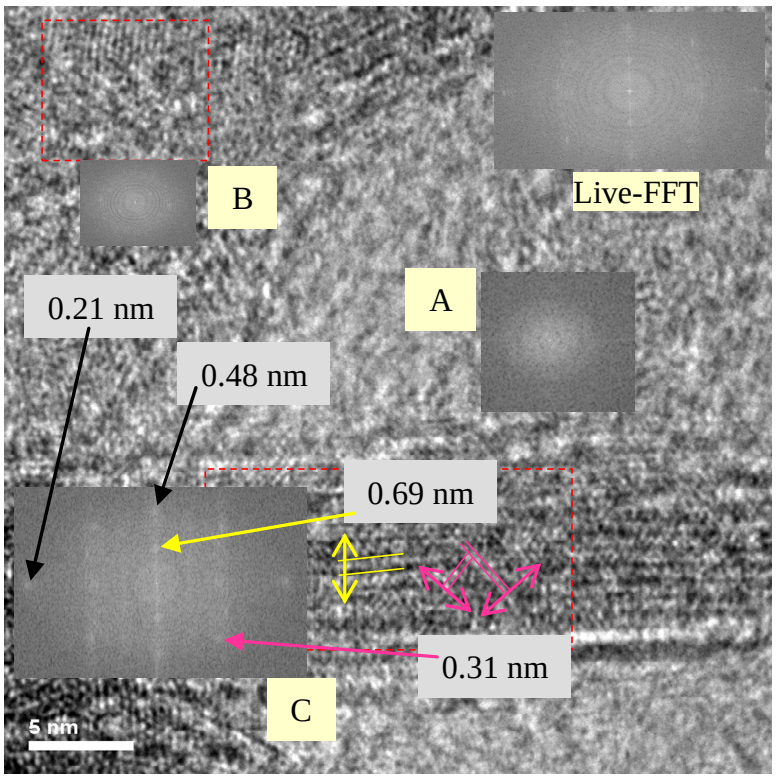

Figure 23. HRTEM image taken at 1MX magnification of the sample V1P78D, which presents a FT of the local ROI that measure 0.69 nm, 0.48 nm, 0.31 nm, and 0.21 nm.

The HRTEM of the sample V1P78D, as shown in Figure 24, presents with regions labeled A, B and C. The live-FFT of the overall “real image” transform (inset image, lower left), indicated randomly distributed lattice planes (e.g. polycrystalline or very small grain material). The overall “real image” and the FFT-micrograph shown in Figure 24 are consistent with multiple lattice fringe orientation, possibly due to crystallite overlap. Region A represents amorphous areas produced by the carbon film that coats the sample support grid. The FT micrographs, shown at Regions B and C, present FT of local regions of interest.

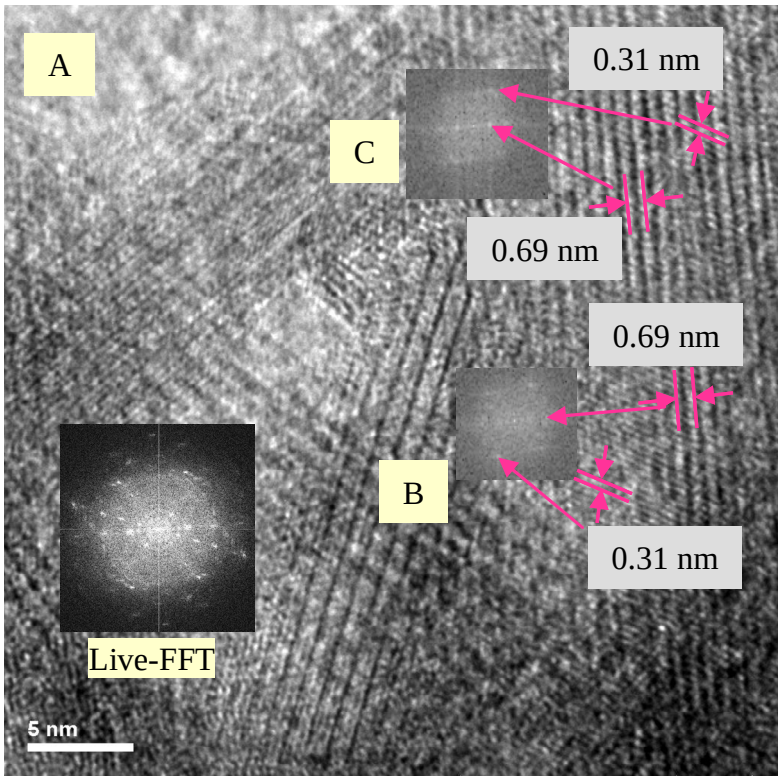

Figure 24. HRTEM image taken at 1MX magnification of the sample V1P78D, which presents direct lattice fringe measurement that were consistent with FT of local ROI measurements of 0.69 nm and 0.31 nm.

Subsequent direct lattice fringe measurement were consistent with the measured regions in the FT of the ROI with measurements corresponding to 0.69 nm and 0.31 nm, which correlated well with XRD pattern d-spacing corresponding to d(110) and d(310), respectively.

CHAPTER 5

CONCLUSIONS

The combined information from XRD and HRTEM analysis for the samples V1P76A, V1P76B, and V1P77C, suggest that the Mn-oxide phases produced were comparable with reference ICDD PDF-2 #87-1497 (reference ICSD 83236), which corresponds to mineral phase Birnessite. The XRD results for the samples agree well for characteristic repeat lattice plane d(001) of about 7 Å, which has been reported by other research scientists [[76],[77]] for Birnessite. Additionally, TEM studies for the samples V1P76A, V1P76B, and V1P77C confirm the mineral phase Birnessite for major peak intensities and minor peak intensity corresponding to d(001), d(110), and d(002), which verifies the XRD analysis. Additionally, the significant morphological features of the samples V1P76A, V1P76B, and V1P77C presented with characteristic features of Birnessite. The morphology of the Birnessite samples suggests thin-layers without discernable pattern of regularity about the edges or in the overlapping of the thin sheets. The microstructure and morphology comparisons as viewed with SEM and TEM of the produced synthetic Birnessite samples were nearly indistinguishable. Thus, for the sample V1P76A, gathered information gained from XRD was confirmed by TEM studies that the Mn-oxide phase of Birnessite was produced using a synthetic procedure involving the reduction of 0.125M $KMnO_4$ promoted by 0.500M hydrochloric acid at room temperature and subsequently wet-aged in the mother liquor for 72 hours. Additionally, for the samples V1P76B and V1P77C gathered information gained from XRD was confirmed by TEM studies confirm that the Mn-oxide phase of Birnessite (δ-MnO_2) was produced using a synthetic procedure involving the reduction of 0.125M

$KMnO_4$ in 3.00M alkali chloride salt solution promoted by 0.500M hydrochloric acid at room temperature subsequently wet-aged in the mother liquor for 72 hours.

Conversely, the combined information from XRD and confirmed by HRTEM analysis for the sample V1P78D suggested that the Mn-oxide phase of Cryptomelane (γ-MnO_2), which was comparable with reference ICDD PDF-2 #77-1796 (reference ICSD 59159), was produced using a synthetic procedure involving the reduction of 0.125M $KMnO_4$ in a 3.00M NaCl solution promoted by 0.500M sulfuric acid at room temperature and subsequently wet-aged in the mother liquor for 72 hours.

It was learned that the influence of alkali chloride salt with variation of its counter cation produces no mineral phase change. In other words, the use of KCl in place of NaCl resulted in no change in crystal structure type. There was no transformation from the layer-structure Birnessite mineral phase into a tunnel-structure Cryptomelane mineral phase and no direct formation of Cryptomelane resulted from the presence of these alkali chloride salts. Samples produced in the presence of 0.500M HCl and 3.00M alkali chloride salt (NaCl or KCl) are Birnessite mineral phase.

The significant contribution of this work presents clarification of the influence of cations and anions on Mn-oxide mineral phase formation/transformation. Coincidentally, the very near-range order of the samples limits any one method to solely identify the mineral phase, thus another contribution is to convey the robust information gained from combination of XRD and TEM studies, which allows for mineral phase identification confirmation.

CHAPTER 6

DISCUSSION

Initially, the rate of the reaction involving KCl appeared to be more vigorous and rapid than for NaCl, however the products were both Birnessite mineral phase. The vigorous reaction in the presence of $K^+ + Cl^-$ under acidic conditions was similar to the reaction involving HSO_4^-. Each reaction of this study progressed quickly to the final products.

Previously, we reported product formation rates for the Cryptomelane [78] and Birnessite [79] formed from classic techniques (McKenzie, 1971). Moreover, in the presence of applied heat (75 ^oC for Cryptomelane synthesis and 100 ^oC for the Birnessite synthesis), both of these reported products formed in 4 h; reproducibility reactions showed that the same products formed in 2 h by increasing the drop-wise rate of addition part of the procedure. Additionally, the Cryptomelane mineral phase formed during the decomposition of permanganate and concentrated sulfuric acid [80], the reaction for which we previously reported began vigorously and then progressed slowly for about a week-and-a-half. Therefore, the current study was designed to explore other parameters that were, basically, the remaining culprits (the cations and anions that were involved in our earlier studies). The classic method we used to produce Birnessite (McKenzie, 1971) involved permanganate, HCl, and applied temperature (100 ^oC during synthesis). The classic method we used to produce Cryptomelane (McKenzie, 1971) involved manganous sulfate ($Mn(II)SO_4$), acetic acid, permanganate, and applied temperature (75 ^oC for Cryptomelane during synthesis). If we removed the applied temperature and then isolated the specific cations (K^+; Na^+ was used as a comparator) and anions (Cl^- versus HSO_4^-),

we could determine the major influencing parameter on the formation of Birnessite versus Cryptomelane mineral phases. Until now, the specific parameter of influence that promotes to formation of Birnessite versus Cryptomelane using syntheses modified from the methods of McKenzie, 1971, has not been reported. We avoided use of Mn(II) because it could interfere with realizing the influence of K^+ or Na^+ in the reaction matrix. Additionally, we wanted to determine if the sulfate rather than $MnSO_4$ (in some way) or the Mn(II) was the influence on Cryptomelane formation. By removing applied temperature and the presence of Mn(II) we could indirectly rule these parameters out if without their presence we formed the Birnessite and Cryptomelane products. In fact, the current study shows that under the present conditions that produced Birnessite, when the reaction occurred in the presence of sulfate, Cryptomelane was formed. It may be possible to replicate such a mineral phase formation/transformation using other anion species, but these are not explored in the present study. Because we were severely limited in funding at this grossly under-represented university, the most likely reaction matrix candidates that ruled out the greatest number of influences could be selected for this study. Certainly there must be many parameters that influence mineral phase formation/transformation; otherwise, how strangely unremarkable would be our natural world. Likewise, this research does not explore kinetics/rates; no interpretation of rates was explored in the data interpretations or the discussion. We do not have direct data for the study of sorption kinetics. Thus, the purpose of the claims made here are not intended as proof of reaction mechanism, but rather to state what may be inferred from the data as some kind of influence of the reaction parameters on mineral phase formation/transformation.

Interestingly, in the formation of Birnessite, [Cl^-] showed no influence or variation of the layered-structure type formation. Furthermore, EDS identified that there was no [Cl^-] in the samples produced. XRD analysis identified the samples as Birnessite-types, which were verified with TEM studies. Conversely, although in high concentration of [Cl^-], the presence of [HSO_4^-] influenced the mineral phase formation; as measured with XRD and verified with TEM studies, it was found to have produced Cryptomelane instead of Birnessite. This suggests that the influence of these anions on mineral phase formation may be different. One possibility is that chloride may not influence the mineral oxide surface under these acidic conditions; the chloride may simply be rapidly forming into chlorine gas. Another explanation is that sulfate under these conditions may complex at the mineral oxide surface. All of these possibilities are supported by research in the field of solid surface-water research. The influence of sulfate to promote Cryptomelane formation may be acting on surface active sites.

A beneficial next study would include *in situ* measurements of phase formation as well as surface potential measurements. It would be fruitful to study sorption phenomenon with *in situ* XRD at various concentrations of sulfate. This would allow for greater understanding of the influence of sulfate and sulfate-based ligands on the formation and development of mineral oxides. Thermodynamic measurements of the solid surface with increased loading of sulfate would be an interesting study. It is an interesting concept, and not without precedent in the literature, that the sulfate may be adsorbed on the surface of the developing Mn-oxide surfaces. Subsequently, metallic or transition metal species are attracted to a mineral oxide surface possessing adsorbed sulfate.

This research adds to our previous research toward understanding influences on mineral phase formation/transformation. Research beyond this thesis is being developed to explore the current topic further. Future direction for this work will involve exploration of surface thermodynamics that are present during phase formation/transformation toward development of an underlying theory that correlates the specific energy (perhaps at surface active sites – surface active site study is unpublished data) to govern formation of tunnel-structure or layer-structure type Mn-oxides. Toward this end, transformation/formation of solid state nanomaterials using *in situ* thermodynamic measurements to study the role of sorption may be an interesting and useful endeavor as well.

REFERENCES

1 W.F. Cole, A.D. Wadsley and A. Walkley, Trans. Electrochem. Society, 1947, 92, 133-158.

2 O. Bricker, The American Mineralogist, 1965, 50, 1296-1355.

3 R.M. McKenzie, Mineralogical Magazine, 1971, 38, 493-502.

4 S.L. Brock, N.G. Duan, Z.R. Tian, O. Giraldo, H. Zhou and S.L. Suib, Chem. Mater. 1998, 10, 2619.

5 V.A. Drits, B. Lanson and A.-C. Gaillot, Am. Mineral, 2007, 92, 771-788.

6 Y.F. Shen, Y.S. Ding, J. Liu, J. Cai, K. Laubernds, R.P. Zerger, A. Vasiliev, M. Aindow and S.L. Suib, Advanced Materials, 2005, 17:7, 805-809. April 4,

7 Y.S. Ding, X.F. Shen, S. Sithambaram, S. Gomez, R. Kumar, V.M.B. Crisostomo, S.L. Suib and M. Aindow, Chemical Materials, 2005, 17, 5382-5389.

8 H. Cao and S.L. Suib, Journal of the American Chemical Society, 1994, 116, 5334.

9 W.E. Richmond and M. Fleischer, American Mineralogist, 1942, 27, 607–610.

10 H.T. Zhang, X.H. Chen, J.H. Zhang, G.Y. Wang, S.Y. Zhang, Y.Z. Long, Z.J. Chen and N.L. Wang, Journal of Crystal Growth, 2005, 280, 292-299.

11 L.H.P. Jones and Angela A. Milne, Mineralogical Magazine, 1956, 31, 283-288.

12 S.L. Brock, M. Sanabria, J. Nair, S.L. Suib and T. Ressler, J. Phys. Chem, 2001, B105, 5404.

13 Y.S. Ding, X.F. Shen, S. Gomez, H. Luo, M. Aindow and S.L. Suib. Advanced Functional Materials, 2006, 16, 549-555.

14 L.H.P. Jones and Angela A. Milne, Mineralogical Magazine, 1956, 31, 283-288.

15 R.M. MacKenzie, Mineralogical Magazine, 1971, 38, 493-502.

16 R.M. Taylor, R.M. McKenzie and K. Norrish, Australian Journal of Soil Research, 1964, 2, 235-248.

17 K.A. Malinger, Y.S. Ding, S. Sithambaram, L. Espinal, S. Gomez and S.L. Suib, Journal of Catalysis, 2006, 239, 290-298.

18 Y.S. Ding, X.F. Shen, S. Sithambaram, S. Gomez, R. Kumar, V.M.B. Crisostomo, S.L. Suib and M. Aindow, Chemical Materials, 2005, 17, 5382-5389.

19 Y.F. Shen, Y.S. Ding, J. Liu, J. Cai, K. Laubernds, R.P. Zerger, A. Vasiliev, M. Aindow and S.L. Suib, Advanced Materials, 2005, 17:7, 805-809.

20 R. Ma, Y. Bando, L. Zhang and T. Sasaki, Adv. Mater. 2004, 16, 918.

21 J.C. Villegas, L.J. Garces, S. Gomez, J.P. Durand and S.L. Suib, Chemical Materials, 2005,.17, 1910-1918.

22 C.L. Lopano, P.J.Heaney, J.E. Post, J. Hanson and S. Komarneni, American Mineralogist, 2007, 92, 380-387.

23 M.A. Cheney, N.R. Birkner, L. Ma, T. Hartmann, P.K. Bhowmik, V.F. Hodge and S.M. Steinberg, Colloids and Surfaces A - Physicochemical and Engineering Aspects, 2006, 289:1-3, 185-192.

24 M.A. Cheney, N.R. Birkner, L. Ma, T. Hartmann, P.K. Bhowmik, V.F. Hodge and S.M. Steinberg, Abstracts of Papers (2006 ACS National Meeting), San Francisco, CA. 232 GEOC 087.

25 M.A. Cheney, P.K. Bhowmik, S. Moriuchi, N.R. Birkner, V.F. Hodge and S.E. Elkouz, Colloids and Surfaces A: Physicochem. Eng. Aspects, 2007, 307, 62–70.

26 C.A. Jacobson, (editor). Encyclopedia of Chemical Reactions. Vol.2. Reinhold Publishing Corporation. 1948.

27 H. Remy. Treatise on Inorganic Chemistry. Vol.1. Elsevier Publishing Company. 1956.

28 Linus Pauling. Inorganic Chemistry. 3rd edition. 1988.

29 O. Bricker, The American Mineralogist, 1965, 50, 1296-1355.

30 R.M. Caven and G.D. Lander, Systematic Inorganic Chemistry. 6th edition. Edited by A. B. Crawford. London and Glasgow: Blackie and Son Limited. 1948.

31 H. Remy. Treatise on Inorganic Chemistry. Vol.1. Elsevier Publishing Company. 1956.

32 W.M. Latimer and J.H. Hildebrand. Reference book of inorganic chemistry. 1st edition. New York, Macmillan Co. 1938.

33 G. Cao, Nanostructures & Nanomaterials. Synthesis, properties and applications. London: Imperial College Press. 2004.

34 M. Tuncay, N. Yuce, B. Arlkan and S. Gokturk, Colloids Surf A. Physicochem. Eng. Aspects. 149:279. 1999.

35 Kabir-ud-Din, S.M.S. Iqubal and Z. Khan, Colloid and Polymer Science, 2005, 283:5; 504-511.

36 J.P. Pretorius and P.W. Linder, Applied Goechemistry, 2001, 16, 1067-1082.

37 J.E. Post, R.B. Von Dreele, and P.R. Buseck, Acta Crystallographica, 1982, B38, 1056-1065.

38 J.E. Post and C.W. Burnham, American Mineralogist, 1986, 71, 1178-1185.

39 R.M. Taylor, R.M. McKenzie and K. Norrish, Australian Journal of Soil Research, 1964, 2, 235-248.

40 W. Stumm and J.J. Morgan, Aquatic Chemistry. (3rd ed.) John Wiley and Sons, Inc. 1996.

41 W.K. Burton, N. Cabrera and E.C. Frank, Trans. Roy. Soc. A, 1950, 243; 299.

42 W. Stumm and J.J. Morgan, Aquatic Chemistry. (3rd ed.) John Wiley and Sons, Inc. 1996.

43 H. Remy, Treatise on Inorganic Chemistry. Vol.1. Elsevier Publishing Company. 1956.

44 R.M. Caven and G.D. Lander. Systematic Inorganic Chemistry. 6th edition. Edited by A. B. Crawford. London and Glasgow: Blackie and Son Limited. 1948.

45 W.M. Latimer and J.H. Hildebrand. Reference book of inorganic chemistry. 1st edition. New York, Macmillan Co. 1938.

46 Linus Pauling. Inorganic Chemistry. 3rd edition. 1988.

47 W. Stumm. Chemistry of the Solid-Water Interface: Processes at the mineral-Water and Particle-Water Interface in Natural Systems. John Wiley & Sons, Inc. 1992. P 23.

48 R.M. McKenzie, Mineralogical Magazine, 1971, 38, 493-502.

49 S. Brunauer, P.H. Emmett and E. Teller, JACS, 1938, 60, 309.

50 https://www-s.nist.gov/srmors/tables/view_table.cfm?table=209-1.htm

51 R.E. Dinnebier and S.J.L. Billinge, Powder Diffraction: Theory and Practice, RSC Publishing, 2008, pp 215-216.

52 M.A. Cheney, P.K. Bhowmik, S. Moriuchi, N.R. Birkner, V.F. Hodge and S.E. Elkouz, Colloids and Surfaces A: Physicochem. Eng. Aspects, 2007, 307, 62–70.

53 S.J.L. Billinge, J. Solid State Chemistry, 2008, 181:7, 1695-1700.

54 R.E. Dinnebier and S.J.L. Billinge, Powder Diffraction: Theory and Practice, RSC Publishing, 2008, pp 215-216: ISBN 0854042318; 9780854042319.

55 D.B. Williams and C.B. Carter, Transmission Electron Microscopy; Diffraction, 1996, Vol. 2.

56 H. Hofmeister, From Nanoparticles to Nanorods and Nanowires: A. Vaseashta et al. (eds.), Nanostructured and Advanced Materials, 2005, pp. 131–138.

57 C.L. Lopano, P.J. Heaney, J.E. Post, J. Hanson and S. Komarneni, Am. Mineral, 2007, 92, 380-387.

58 V.A. Drits, B. Lanson and A.-C. Gaillot, Am. Mineral, 2007, 92, 771-788.

59 H.T. Zhang, X.H. Chen, J.H. Zhang, G.Y. Wang, S.Y. Zhang, Y.Z. Long, Z.J. Chen and N.L. Wang, Journal of Crystal Growth, 2005, 280, 292-299.

60 M. Villalobos, B. Lanson, A. Manceau, B. Toner and G. Sposito, Am. Mineral. 2006, 19, 489.

61 J.C. Villegas, L.J. Garces, S. Gomes, J.P. Durand and S.L. Suib, Chem. Mater., 2005, 17, 1910.

62 B. Toner, S. Fakra, M. Villalobos, T. Warwick and G. Sposito, Appl. Envirom. Microbiol, 2005, 71, 1300.

63 L.-Z. Ma, T. Hartmann, M. Cheney, N.R. Birkner, P. Bhowmik, Microsc. Microanal, 2008, 14, 1–7.

64 M.A. Cheney, P.K. Bhowmik, S. Moriuchi, N.R. Birkner, V.F. Hodge and S.E. Elkouz, Colloids and Surfaces A: Physicochem. Eng. Aspects, 2007, 307, 62–70.

65 A.-C. Gaillot, V.A. Drits, A. Plançon and B. Lanson, Chemistry of Materials, 2004, 16, 1890-1905.

66 I.N. Demchenko, K. Lawniczak-Jablonska, T. Tyliszczak, N.R. Birkner, W.C. Stolte, M. Chernyshova and O. Hemmers, J. of Electron Spec. and Rel. Phenom., 2009, 171, 24-29.

67 A.-C. Gaillot, V.A. Drits, A. Plançon and B. Lanson, Chemistry of Materials, 2004, 16, 1890-1905.

68 M. Faller, University of Berne, Berne, Switzerland., Private Communication, 1989; H. Kudo, H. Miura and Y. Hariya, J. Mineral., 1990, 15, 50; R. Giovonoli and M. Faller, Chimia, 1989, 43, 54.

69 Y. Lin, X. Cui and L. Li, Electrochem. Commun., 2005, 7, 166.

70 J. Vicat, E. Fanchon, P. Strobel and D. Tran Qui. Acta Crystallographia, Section B: Structural Science. 1986, B42:2, 162-167.

71 L. Wang, K. Takada, A. Kajiyama, M. Onoda, Y. Michiue, L. Zhang, M. Watanabe and T. Sasaki, Chem. Mater., 2003, 15, 4508; L. Wang, T. Sasaki, Y. Ebina, K. Kurashima and M. Watanabe, Chem. Mater., 2002, 14, 4827; T. Sasaki, Y. Ebina, Y. Kitami and M. Watanabe, J. Phys. Chem. B, 2001, 105, 6116; T. Sasaki and M. Watanabe, J. Phys. Chem. B, 1997, 101, 1015-9; T. Sasaki, S. Nakano, S. Yamauchi and M. Watanabe, Chem. Mater., 1997, 9, 602.

72 V.A. Drits, B. Lanson and A.-C. Gaillot, American Mineralogist, 2007, 92:771-788.

73 M. Villalobos, B. Lanson, A. Manceau, B. Toner and G. Sposito, Am. Mineral. 2006, 19, 489.

74 H. Hofmeister. From Nanoparticles to Nanorods and Nanowires: A. Vaseashta et al. (eds.), Nanostructured and Advanced Materials, 2005, pp. 131–138.

75 L.-Z. Ma, T. Hartmann, M. Cheney, N.R. Birkner, P. Bhowmik, Microsc. Microanal, 2008, 14, 1–7.

76 V.A. Drits, B. Lanson and A.-C. Gaillot, Am. Mineral, 2007, 92, 771-788.

77 A.-C. Gaillot, V.A. Drits, A. Plançon and B. Lanson, Chemistry of Materials, 2004, 16, 1890-1905.

78 M.A. Cheney, N.R. Birkner, L. Ma, T. Hartmann, P.K. Bhowmik, V. F. Hodge and S.M. Steinberg, Colloids and Surfaces A - Physicochemical and Engineering Aspects, 2006, 289:1-3, 185-192.

79 M.A. Cheney, N.R. Birkner, L. Ma, T. Hartmann, P.K. Bhowmik, V.F. Hodge and S.M. Steinberg, Presentation of Papers (2006 ACS National Meeting), San Francisco, CA. 232 GEOC 087.

80 M.A. Cheney, P.K. Bhowmik, S. Moriuchi, N.R. Birkner, V.F. Hodge and S.E. Elkouz, Colloids and Surfaces A: Physicochem. Eng. Aspects, 2007, 307, 62–70.

VITA

Graduate College
University of Nevada, Las Vegas

Nancy R. Birkner

Degrees:
Bachelor of Arts, Chemistry, 1993
University of Nevada, Las Vegas

Honors and Awards:
National Dean's List (15th annual edition)
Phi Theta Kappa International Academic Honor Society
Golden Key International Honor Society, 2008
Nominated for the International Scholar Laureate Program, 2009

Publications:

1. Publication (Refereed and Archival Journals): I.N. Demchenko, K. Lawniczak-Jablonska, T. Tyliszczak, N.R. Birkner, W.C. Stolte, M. Chernyshova, O. Hemmers, "XANES studies of modified and newly synthesized nanostructured manganese oxides", *J. of Electron Spec. and Rel. Phenom.*, 2009, 171, 24-29.
2. Publication (Refereed and Archival Journals): L.-Z. Ma, T. Hartmann, M. Cheney, N.R. Birkner, P. Bhowmik, "Characterization of an Inorganic Cryptomelane Nanomaterial Synthesized by a Novel Process Using Transmission Electron Microscopy and X-Ray Diffraction", *Microsc. Microanal, 2008, 14, 1–7.*
3. 235th ACS National Conference in New Orleans, LA (2008): N.R. Birkner, S.M. Steinberg, T. Hartmann, L.-Z. Ma, R.J. Fairhurst, "Atomic resolution microanalysis of inorganic nanostructure materials", (ACS National Meeting), New Orleans, LA. *235* INORG 1157604.
4. Publication (Refereed and Archival Journals): M.A. Cheney, P.K. Bhowmik, S. Moriuchi, N.R. Birkner, V.F. Hodge and S.E. Elkouz, "Synthesis and characterization of two phases of manganese oxide from decomposition of permanganate in concentrated sulfuric acid at ambient temperature", *Colloids and Surfaces A: Physicochem. Eng. Aspects*, 2007, 307, 62–70.
5. 63rd ACS Southwestern Regional Meeting in Lubbock, Texas (SWRM 2007): *N.R. Birkner*, S.M. Steinberg, R.J. Fairhurst , T. Hartmann , L.-Z. Ma, "Synthesis and characterization of nanostructure Mn-oxide-based crystal balls, strings, and rods: what's in your oxide?", INORG.
6. 233rd ACS National Conference in Boston, Massachusetts (2007): *Spencer M. Steinberg* and Nancy R. Birkner, "Formation of organic iodine in soil and sediment by reaction of Manganese-oxides with iodide".

7. Microscopy and Microanalysis Conference in Chicago, Illinois (2006): L. Ma, T. Hartmann, M.A. Cheney, N.R. Birkner, "Micro-structural characterization of inorganic cryptomelane nanorods using transmission electron microscopy, electron- and X-ray spectroscopy, and X-ray diffraction". *Microsc. Microanal, 2006, 12; SUPPL. 2:740-1*.
8. 232nd ACS National Conference in San Francisco, California (2006): M.A. Cheney, *N.R. Birkner*, L. Ma, T. Hartmann, P.K. Bhowmik, V.F. Hodge, S.M. Steinberg, "Synthesis and characterization of inorganic double helices of cryptomelane nanomaterials". *General Paper (ACS National Meeting)*, San Francisco, CA. *232* GEOC 39.
9. Publication (Refereed and Archival Journals): M.A. Cheney, N.R. Birkner, L. Ma, T. Hartmann, P.K. Bhowmik, V. F. Hodge, S.M. Steinberg, "Synthesis and characterization of inorganic double helices of cryptomelane nanomaterials", *Colloids and Surfaces A - Physicochemical and Engineering Aspects*, 2006, 289:1-3, 185-192.
10. 232nd ACS National Conference in San Francisco, California (2006): M.A. Cheney, N.R. Birkner, L. Ma, T. Hartmann, P.K. Bhowmik, V.F. Hodge, S.M. Steinberg, "Novel synthesis of layer-structured black birnessite nanomaterial from brown birnessite with complex shape under controlled oxygen and acidic conditions". *Presentation of Paper (ACS National Meeting)*, San Francisco, CA. *232* GEOC 087.
11. Publication (Refereed and Archival Journals): M.A. Cheney, N.R. Birkner, L. Ma, T. Hartmann, P.K. Bhowmik, V.F. Hodge, S.M. Steinberg, "Novel synthesis of layer-structured black birnessite nanomaterial from brown birnessite with complex shape under controlled oxygen and acidic conditions" (*2006, in review, Colloids and Surfaces A - Physicochemical and Engineering Aspects*).

Thesis title: Manganese Oxide Mineral Phases Produced at Room Temperature under Acidic Conditions Investigated with XRD, TEM, SEM, EDS and BET

Thesis Examination Committee:
Chairperson, Spencer M. Steinberg, Ph.D.
Committee Member, Thomas Hartmann, Ph.D.
Committee Member, Longzhou Ma, Ph.D.
Committee Member, Dennis W. Lindle, Ph.D.
Committee Member, Clemens Heske, Ph.D.
Graduate College Representative, Andrew Cornelius, Ph.D.